



TECHNISCHE
UNIVERSITÄT
WIEN

DIPLOMARBEIT

Surface science studies of model IrO_2 and $\text{Rh}_1/\text{Fe}_2\text{O}_3$ catalysts

ausgeführt am Institut für Angewandte Physik
der Technischen Universität Wien

unter der Anleitung von

Prof. Gareth S. Parkinson

durch

Nikolaus Resch

Matrikelnummer 09871351

Wien, 25.07.2020

Nikolaus Resch

Gareth Parkinson



Die approbierte gedruckte Originalversion dieser Diplomarbeit ist an der TU Wien Bibliothek verfügbar.
The approved original version of this thesis is available in print at TU Wien Bibliothek.



Die approbierte gedruckte Originalversion dieser Diplomarbeit ist an der TU Wien Bibliothek verfügbar.
The approved original version of this thesis is available in print at TU Wien Bibliothek.



Die approbierte gedruckte Originalversion dieser Diplomarbeit ist an der TU Wien Bibliothek verfügbar.
The approved original version of this thesis is available in print at TU Wien Bibliothek.

Acknowledgements

I'd like to thank Peter for showing me the ins and outs of RT

Sarah and Sebastian for their great company and help in the lab

Michele and Giada for their patience and assistance

Michael for being an inexhaustible well of knowledge and repairing all the things

Florian for his expertise and friendship

And of course

Gareth for giving me the opportunity to work in such an awesome group

Abstract

Metal oxides play an important role in the field of catalysis, both as a catalytically active substance and as a support material. An in depth understanding of surfaces on an atomic level is key for designing selective, viable catalytic systems.

Using an ultra-high vacuum (UHV) chamber setup, two metal oxide systems (IrO_2 and $\alpha\text{-Fe}_2\text{O}_3$) are studied using surface science methods including low energy electron diffraction (LEED), X-ray photoelectron spectroscopy (XPS) and scanning tunnelling microscopy (STM).

XPS measurements on an IrO_2 single crystal reveal a shift of the Ir 4f peak to higher binding energies when annealed in oxygen ($T = 450\text{ }^\circ\text{C}$, $p_{\text{O}_2} > 5 \times 10^{-5}\text{ mbar}$) compared to the sputtered surface. The spectra always show a contribution from metallic Ir and a higher binding energy contribution associated with oxidized iridium. The position of the metallic peak shifts $\approx 0.4\text{ eV}$ towards higher binding energies during annealing while the oxide peak only shifts by $\approx 0.2\text{ eV}$. STM studies on the same crystal show the existence of two different atomic surface structures. One of these structures (rectangular unit cell, $a \times b = 0.55 \times 0.45\text{ nm}^2$, found on rectangular-shaped terraces) was identified as the $\text{IrO}_2(101)$ surface, which is confirmed with electron backscatter diffraction (EBSD) measurements. It shows a (1×1) periodicity like the bulk truncated surface. The other structure (hexagonal or rhombic unit cell, $a = b = 0.55\text{ nm}^2$, found on triangular-shaped terraces) has not been clearly identified. Possible candidates include the $\text{IrO}_2(111)$ surface, an oxygen overlayer on metallic $\text{Ir}(111)$ or a contamination-induced surface reconstruction.

Experiments on hematite ($\alpha\text{-Fe}_2\text{O}_3$) were conducted on a natural crystal sample as well as on homoepitaxial thin film samples with various titanium-doping percentages (3.1 at%, 0.8 at% and 0.03 at%). A hematite thin film with a titanium doping level of 0.03 at% was produced using pulsed laser deposition (PLD) and proved to be suitable for surface science studies.

Different coverages (0.2 monolayers (ML), 0.05 ML) of rhodium were deposited on the hematite (012) (1×1) surface and annealed at progressively higher temperatures (up to $570\text{ }^\circ\text{C}$). Annealing at $300\text{ }^\circ\text{C}$ and $400\text{ }^\circ\text{C}$ leads to a decrease in areal density of Rh-related protrusions on all samples in STM, consistent with an agglomeration into larger clusters. The protrusion height measured with STM on the samples with 0.05 ML of Rh does not increase when heating in UHV. This suggests an incorporation rather than a sintering process for these coverages. The XPS peak fit of the Rh 3d region shows an increased contribution of the peak associated with oxidized Rh when the annealing temperature is increased, consistent with incorporation into the hematite lattice. After annealing at $500\text{ }^\circ\text{C}$ the surface appears without protrusions in STM, while oxidized Rh species remain visible in XPS.

On the undoped crystal with 0.2 ML Rh, in contrast to the bare surface, multiple annealing cycles in UHV were unsuccessful to prepare the (2×1) reconstruction, as confirmed with LEED measurements. On the 0.03 at% Ti-doped thin film with 0.05 ML Rh, the (2×1) reconstruction could only be prepared on the hotter part of the crystal. These results suggest that the incorporated Rh stabilizes the (1×1) surface.

Kurzfassung

Metalloxide spielen eine wichtige Rolle in der heterogenen Katalyse, und zwar sowohl als Trägermaterialien als auch als die katalytisch aktiven Komponenten. Für die Entwicklung hochselektiver Katalysatoren ist ein grundlegendes Verständnis der Oberflächen auf atomarer Skala von Nutzen.

In einer Ultrahochvakuum-Kammer wurden die zwei Metalloxid-Systeme IrO_2 und $\alpha\text{-Fe}_2\text{O}_3$ mit oberflächenphysikalischen Methoden untersucht. Dabei kamen die Beugung niederenergetischer Elektronen (LEED), Röntgenphotoelektronenspektroskopie (XPS) und Rastertunnelmikroskopie (STM) zum Einsatz.

XPS-Messungen eines IrO_2 -Einkristalls nach Erhitzen in Sauerstoff ($T = 450\text{ °C}$, $p_{\text{O}_2} > 5 \times 10^{-5}\text{ mbar}$) zeigen im Vergleich zur gesputterten Oberfläche eine Verschiebung des Ir 4f Peaks zu höheren Bindungsenergien. Alle Spektren weisen eine metallische Ir-Komponente und eine Komponente bei höheren Bindungsenergien auf, die oxidiertem Iridium zugeordnet wurde. Während des Heizprozesses verschiebt sich die Position des metallischen Peaks um $\approx 0,4\text{ eV}$ in Richtung höherer Bindungsenergien, die Position des oxidischen Peaks verschiebt sich hingegen nur um $\approx 0,2\text{ eV}$. STM-Untersuchungen auf demselben Kristall zeigen zwei verschiedene Oberflächenstrukturen. Die erste Struktur (rechteckige Einheitszelle, $a \times b = 0,55 \times 0,45\text{ nm}^2$, beobachtet auf rechteckigen Terrassen) wurde als $\text{IrO}_2(101)$ Oberfläche identifiziert, was auch mittels Elektronenrückstreubeugung (EBSD) bestätigt werden konnte. Analog zur bulk-terminierten Oberfläche weist diese Struktur eine (1×1) Periodizität auf. Die zweite Struktur (hexagonale oder rhombische Einheitszelle, $a = b = 0,55\text{ nm}^2$, beobachtet auf dreieckigen Terrassen) konnte nicht eindeutig identifiziert werden. Möglicherweise handelt es sich um die $\text{IrO}_2(111)$ Oberfläche, eine Sauerstoffschicht auf metallischem Ir(111) oder eine durch Kontaminationen verursachte Oberflächenrekonstruktion.

Experimente auf Hämatit ($\alpha\text{-Fe}_2\text{O}_3$) wurden auf einem natürlichen Einkristall und auf homoepitaxialen Dünnschichtproben mit unterschiedlichen Titan-Dotierungen (3,1 at%, 0,8 at% und 0,03 at%) durchgeführt. Eine Hämatit-Dünnschichtprobe mit einem Titan-Dotierungsgehalt von 0,03 at% wurde mittels Laserstrahlverdampfen hergestellt und erfolgreich für oberflächenphysikalische Untersuchungen eingesetzt.

Auf die Hämatit (012) (1×1) Oberfläche wurden unterschiedliche Bedeckungen (0,2 Monolagen (ML) und 0,05 ML) von Rhodium aufgetragen und anschließend schrittweise auf höhere Temperaturen (bis zu 570 °C) erhitzt. STM-Messungen zeigen, dass ein Heizen der Proben auf 300 °C und 400 °C zu einer niedrigeren Flächendichte der durch Rh verursachten Erhebungen führt. Dieses Ergebnis kann mit der Bildung von Clustern erklärt werden. Die mit STM vermessenen Höhen der Erhebungen auf den Proben mit 0,05 ML Rh nehmen selbst nach Erhitzen der Probe im Ultrahochvakuum nicht zu. Dies deutet darauf hin, dass anstelle eines Sinter-Prozesses eine Inkorporation stattfindet. Ein Peak-Fit Verfahren des Rh 3d Bereichs der XPS Spektren zeigt, dass mit steigender Proben temperatur oxidiertes Rh einen stärkeren Beitrag liefert. Dies kann als Hinweis auf die Inkorporation von Rh in das Hämatit-Gitter interpretiert werden. Nach Erhitzen der Proben auf 500 °C wurden im Rastertunnelmikroskop keine Erhebungen auf der Probe mehr festgestellt, obwohl in den XPS Spektren der Rhodiumoxid-Peak weiterhin aufschien.

Aus LEED Messungen ist ersichtlich, dass auf dem undotierten Kristall mit einer Bedeckung von 0,2 ML Rh die Präparation der (2×1) Rekonstruktion trotz mehrfacher Heizvorgänge nicht erzielt wurde. Auf der Dünnschichtprobe mit einem Dotierungsgrad von 0,03 at% und einer Bedeckung von 0,05 ML Rh konnte die (2×1) Rekonstruktion nur auf der heißeren Kristallseite präpariert werden. Dieses Ergebnis lässt die Schlussfolgerung zu, dass inkorporiertes Rh die (1×1) Oberfläche stabilisiert.

Contents

Abstract	iii
Kurzfassung	v
1. Introduction.....	1
2. Experimental Methods	3
2.1 X-ray Photoelectron Spectroscopy	3
2.2 Low Energy Electron Diffraction.....	3
2.3 Scanning Tunnelling Microscopy	5
2.4 Atomic Force Microscopy.....	6
2.5 Scanning Electron Microscope.....	6
2.6 Electron Backscatter Diffraction	7
2.7 Pulsed Laser Deposition.....	7
3. Experimental Setup.....	9
4. Iridium Oxide – IrO ₂	11
4.1 Introduction and Motivation.....	11
4.2 Sample.....	12
4.3 Results	15
4.3.1 XPS data	15
4.3.2 AFM data	18
4.3.3 EBSD data	19
4.3.4 STM data	21
4.4 Discussion	25
4.5 Summary and Outlook	30
5. Hematite – α -Fe ₂ O ₃	31
5.1 Introduction and Motivation.....	31
5.2 Samples	33
5.2.1 Growth process	34
5.2.2 Sample preparation	36
5.3 Results	38
5.3.1 The clean surface	38
5.3.2 Surface defects.....	40
5.3.3 Rhodium deposition.....	43
5.4 Discussion	55
5.5 Summary and Outlook	59
References.....	61

1. Introduction

Catalysis describes the process of altering the kinetics of a chemical reaction. This can be done to change the rate of a reaction, affect the selectivity of a reaction or enable a reaction altogether. The substances used to do so are called catalysts. It is impossible to think about modern industry without catalysis, it is often stated that up to 90 % of all chemical products have catalytic processes involved in their manufacture [1].

In almost any given scenario, the chemical reaction takes place on the surface of the catalyst. To achieve custom-tailored catalysts for real life applications, a deep understanding of both the support material and the catalytic active substance is required. Since catalytic systems in application are often highly complex, the surface science approach aims to selectively reduce the complexity by investigating model systems in a carefully controlled setting. Once processes on an atomic level are well understood under such controlled conditions, the system can be adapted step by step to mimic more realistic conditions and environments. The various experimental techniques are frequently accompanied and complemented by theoretic calculations resulting in a thorough understanding of all the processes involved.

In this work, experimental data gathered from two different systems will be discussed. First, experimental data on an iridium oxide single crystal are presented. Iridium oxide is a prime candidate for the oxygen evolution reaction (OER) and is frequently used in many industrial applications, while thorough understanding of the single crystal surface – especially on an atomic level – is still lacking. This work will present preliminary data combining various surface science techniques aiming for a better understanding of the crystal surface.

The second system discussed is the hematite (012) surface. In industry, the catalytically active material (often noble-metals) are usually dispersed on an inexpensive support, such as iron oxide, to maximize the active sites of the – often expensive – catalytic material. When reducing the particle size of the catalytic material, the catalytic activity and selectivity has been shown to increase [2–4]. Taking this concept to its limits, one arrives at single atoms as the smallest possible nano particle. SAC theoretically represents ultimate efficiency as ideally 100% of the catalytic material is available as an active site. This poses a challenge to the selection of the support material which must stabilize the adsorbed particles through strong bonding sites [5]. Hematite is an oft used support in single-atom catalysis (SAC), but it is not clear how the metal atoms are stable on its surfaces. Previous studies have already led to a good understanding of

the hematite (012) surface on an atomic level, and this work aims to explore the fabrication of surface defects and the introduction of rhodium adatoms on the hematite (012) (1×1) surface.

2. Experimental Methods

In this section, the theoretical basics of the experimental methods used for this work are discussed briefly. An overview on X-ray photoelectron spectroscopy (XPS), low energy electron diffraction (LEED), scanning tunnel microscopy (STM), atomic force microscopy (AFM) and pulsed laser deposition (PLD) is given. Additionally, the principle of a scanning electron microscope (SEM) and electron backscatter diffraction (EBSD) are discussed.

2.1 X-ray Photoelectron Spectroscopy

X-ray photoelectron spectroscopy (XPS) is a technique used to measure the elemental composition of a material. Besides, information about the electronic and chemical state of the element can be obtained. The sample is irradiated with an X-ray beam and the kinetic energy distribution of the emitted electrons is measured.

Using equation 2.1, the binding energy of the sample can be determined.

$$E_b = h\nu - E_{kin} - \varphi_{spec} \quad (2.1)$$

Where E_b is the binding energy, $h\nu$ is the energy of the incident radiation and φ_{spec} is the work function of the detector.

The measured core binding energies are determined by the interaction between the electron and the nucleus and are reduced by the electrostatic shielding effect of other electrons in the atom. If charge is removed or added this shielding effect is altered. Oxidation of an atom leads to a withdrawal of valence electron charge, which in turn increases the measured binding energy. Because of this effect, the metal peak of an oxidized cation is typically shifted to higher binding energies compared to the peak of the pure metal.

Although the incident radiation has a penetration depth in the range of micrometres, most detected electrons originate near the surface of the material, as the mean free path length of the electrons in the sample is very small. Although spatial resolution is low, as it is limited by the optics of the incident X-ray beam as well as by acceptance characteristics of the analyser, the exponentially surface weighted signal can, in theory, be used to get a depth profile of the sample.

2.2 Low Energy Electron Diffraction

Low energy electron diffraction (LEED) is a technique used to determine the surface structure of a material.

A filament emits electrons which are accelerated towards the sample and focused with electromagnetic lenses. The de Broglie wavelength (equation 2.2) of the electrons should be in the same regime as the atomic distances on the surface (around 0.1 nm), which means an energy of 20-200 eV for the electrons.

$$\lambda = \frac{h}{\sqrt{2mE}} \quad (2.2)$$

λ ... wavelength
 m ... mass
 E ... energy
 h ... Planck constant

Interaction with solid matter is especially strong for low energy electrons. The intensity of the beam undergoes an exponential decay in the sample due to inelastic scattering processes – such as plasmon and phonon excitations as well as electron-electron interactions – which results in a very low penetration depth of the incident beam. This makes the technique very surface sensitive.

If sufficient geometric order exists on the surface, the diffraction pattern of the elastically backscattered electrons is recorded, usually using a hemispherical fluorescent screen.

The scattered electrons interfere constructively if the Laue relation is fulfilled. (equation 2.3)

$$k - k_0 = G_{hkl} \quad (2.3)$$

k_0 ... incident wave vector
 k ... scattered wave vector
 G_{hkl} ... vector of the reciprocal lattice

In case of diffraction from a surface, equation 2.3 can be rewritten in the 2-dimensional form (equation 2.4).

$$k^{\parallel} - k_0^{\parallel} = G_{hk} \quad (2.4)$$

Where k^{\parallel} and k_0^{\parallel} are the components of the respective wave vectors parallel to the sample surface and G_{hk} is a 2d-reciprocal lattice vector.

The condition (2.4) gives a pattern of lines which is transformed into a point pattern via a hemispherical screen. Since the observed pattern is a direct picture of the reciprocal lattice on the surface, analysis of the spot positions gives information on the symmetry of the surface structure in real space. In the presence of an adsorbate the qualitative analysis may reveal information about the size and rotational alignment of the adsorbate unit cell with respect to the substrate unit cell.

The number of spots on the screen increases with higher incident beam energy. Bigger real space unit cells increase the number of spots as well, as larger lattice vectors in real space correspond to smaller ones in reciprocal space, which means more reciprocal lattice vectors can fulfil the Laue condition.

2.3 Scanning Tunnelling Microscopy

Scanning tunnelling microscopy (STM) is a technique used for imaging of surfaces on an atomic level. It is based on the quantum-mechanical tunnelling effect, which states that particles can “tunnel” through an – in the classical sense – insurmountable potential barrier with a certain probability.

A conductive tip is brought very close to the sample (typical tip-sample distances are around 0.5 nm) and a voltage, usually referred to as tunnelling bias, is applied between tip and surface. Due to the exponential relation between the tunnelling current (I) and the distance between tip and sample (equation 2.5), it is possible to detect very small changes in height.

$$I \propto e^{-2\kappa d} \quad (2.5)$$

$$\kappa = \sqrt{\frac{2m(U-E)}{\hbar}} \quad (2.6)$$

- κ ... decay length
- d ... distance
- m ... electron mass
- U ... potential barrier
- E ... energy

The tip is scanned over the sample surface in x and y directions while either the z position of the tip or the tunnelling current is held constant. From the measured current, a height profile of the surface can be reconstructed. The tunnelling current is not only dependent on the tip-sample distance but also on the density of states on the surface. This can complicate the interpretation of the measured height profile, especially when the surface and hence the density of states on the surface is unknown.

Unlike other microscopy techniques, STM is not limited in resolution by the wavelength of the probing particle. Moreover, non-periodic structures can be studied contrary to diffraction-based techniques such as LEED. Because the technique relies on measuring a current, the sample must be conductive. Non-conductive samples can either be coated in a conductive metal such as gold or put on a conductive substrate as a thin film to make measurement possible.

2.4 Atomic Force Microscopy

Atomic force microscopy (AFM) is a technique used for imaging of surfaces. Under ultra-high vacuum conditions atomic resolution of the sample surface can be achieved.

A cantilever with a sharp tip is brought close to the sample surface. Forces between the sample and the tip lead to a deflection of the cantilever. This deflection is measured most commonly by beam-deflection of a laser reflected from the cantilever. As the cantilever is scanned over the sample surface, the deflected laser spot generates a signal on a photodiode which is used to generate an image of the surface.

Different imaging modes for AFM exist and can be grouped into three categories: contact mode, non-contact mode and tapping mode.

In contact mode the probing tip is in direct contact with the surface. Either the distance of the cantilever to the surface is kept constant (constant height mode) and the deflection of the cantilever is measured, or a feedback loop regulates the sample-probe distance, keeping the deflection of the cantilever at a constant value (constant force mode).

In non-contact mode the cantilever oscillates near the sample surface at or close to its resonant frequency. As some atomic forces such as the Van-der-Waals force extend above the surface, the oscillating frequency is affected by the surface. A feedback loop regulates the sample-probe distance, keeping the oscillating frequency or amplitude at a constant value.

Tapping mode imaging is performed by monitoring the oscillation amplitude and phase of the cantilever. The cantilever is driven to oscillate near its resonance frequency. The probe tip lightly contacts the sample during the cantilever oscillation. The forces acting on the cantilever close to the surface lead to a change of the resonant frequency of the system resulting in an amplitude change and a phase shift between the exciting signal and the oscillation of the cantilever. A feedback loop adjusts the height of the cantilever maintaining a set cantilever oscillation amplitude.

2.5 Scanning Electron Microscope

A scanning electron microscope (SEM) is an electron microscope where a focused electron beam is scanned over a sample resulting in local excitations. Emitted electrons and photons are measured to gain information about the surface topography and the chemical composition of the sample.

Most commonly, low energy secondary electrons are used for imaging surfaces. Inelastic scattering interactions between the electrons of the primary beam and the electrons of the

sample atoms lead to an emission of secondary electrons. Due to the low energy, and therefore small mean free path length of secondary electrons, excitations deeper than a few nanometres do not contribute to the measured signal, which makes the method very surface sensitive. To measure the secondary electrons, they are first collected using a positively biased grid and then accelerated towards a scintillator. A photomultiplier amplifies the signal resulting in a measured intensity of secondary electrons.

Besides secondary electrons, which are mainly used to image the topography of a surface, backscattered electrons can also be detected. Since heavy elements backscatter electrons more strongly than light elements, the resulting images show a contrast between areas with different chemical compositions. As both the detection angle and the electron energy are different from secondary electrons, a separate detector must be used.

2.6 Electron Backscatter Diffraction

In electron backscatter diffraction (EBSD), the electron beam of a scanning electron microscope is diffracted by atomic layers in the sample. When the diffracted electrons hit a phosphor screen in the detector, they form a distinct pattern consisting of so-called Kikuchi bands. These lines are the result of the projection of Kossel cones, which are formed by all possible directions of Bragg reflection from a lattice plane. The patterns are digitalized and processed to discern the individual Kikuchi lines.

Thus, information about the crystalline structure and crystallographic orientation can be obtained when comparing the recorded patterns to databases.

As a large angular tilt of the sample ($\approx 70^\circ$ compared to normal incidence) is required to maximize the intensity of backscattered electrons, the information depth of the technique is in the range of 20 nm.

2.7 Pulsed Laser Deposition

Pulsed laser deposition (PLD) is a physical vapor deposition technique which has been proven capable of generating high-quality epitaxial films. An intense laser pulse is focused on the target material which leads to a local vaporisation. The evaporated particles form a plasma plume which provides a material flux required for film growth on a substrate. Typically, an ultraviolet (UV) laser with a nanosecond pulse width is used. As PLD is compatible with high background pressures (up to 1 mbar) the growth process can be supplemented by a reactive gas which may affect the ablation plume species in the gas phase or the surface reaction on the substrate. A stoichiometric transfer from multi-cation targets is achievable for many materials

given the right deposition conditions. This makes PLD especially attractive for complex multicomponent film growth.

PLD enables a shot-to-shot control of the deposition process. The time between pulses is high in comparison to the actual deposition time which allows for surface diffusion and aggregation of the deposited species. In-situ techniques such as reflection high-energy electron diffraction (RHEED) can be used to monitor the growth process, allowing for a sub monolayer control of the resulting film.

3. Experimental Setup

Most of the experiments presented in this work were performed in a versatile ultra-high vacuum chamber designed mainly around an STM which operates at room temperature (RT-STM).

The system consists of a sample preparation chamber and a measurement chamber (main chamber) which are separated by a gate valve. Additionally, a small load lock chamber is connected to the preparation chamber, which allows for inserting and extracting samples without the need to vent the whole system.

The preparation chamber is equipped with an electron beam evaporator setup (Omicron), a single metal evaporator, a custom-made zirconium sputter source, an electron gun for heating the sample holder, a quadrupole mass spectrometer (Balzers) and several leak valves for dosing gases (O_2 , Ar, CO, H_2).

The main chamber houses an Omicron μ STM operated in constant current mode, a LEED module (VSI), a commercial XPS setup (X-Ray source (VG) and hemispherical analyser (SPECS Phoibos 100)), an AES setup (electron gun plus a cylindrical analyser (Perkin-Elmer)), a separate electron gun (SPECS), an ion gun (SPECS) and a quadrupole mass spectrometer (Balzers).

Typical base chamber pressures are $< 1.0 \times 10^{-10}$ mbar for the preparation chamber and $< 0.7 \times 10^{-10}$ mbar for the main chamber. When dosing gases in the preparation chamber, it is possible to reach pressures up to 5×10^{-6} mbar. A large turbomolecular pump assures a quick pumping process of the chamber once the leak gas valves have been closed.

4. Iridium Oxide – IrO₂

4.1 Introduction and Motivation

Iridium dioxide is a transition metal dioxide which crystallizes in a tetragonal rutile structure ($a = b = 0.4505$ nm, $c = 0.316$ nm) [6]. It is black of colour both in powder and crystal form and electrically conductive at room temperature. Iridium oxide finds uses as oxidation resistant field emitters, as a durable electrode material in ferroelectric memory devices and is a promising electrochromic material [7,8]. Also, it provides attractive electrochemical properties and is among the most promising candidates as an electrocatalyst for the oxygen evolution reaction ($2 \text{H}_2\text{O} \rightarrow 2 \text{O} + 4 \text{H}^+ + 4 \text{e}^-$) [9,10].

As this reaction is studied intensively to generate fossil-fuel-independent energy carriers, it is a common theme among studies on IrO₂.

Most surface science studies on IrO₂ were conducted on grown thin films. Multiple methods to prepare such thin film samples have been proven to be effective and have been studied intently. Polycrystalline thin films have been grown using cathodic sputtering techniques, DC reactive sputtering techniques and pulsed laser deposition [11–15]. Throughout these studies, deposition temperature and oxygen pressure are among the most important parameters to influence properties of the thin films such as conductivity and roughness. XRD measurements also revealed a strong influence of the deposition parameters on the dominant crystalline phase. More recently, alternative methods such as atomic layer deposition (studied for applications connected to random access memory devices [16]) and metal organic chemical vapour deposition [17] have been proven successful to deposit IrO₂. The latter method excels in growing crystalline nano rods that show promising field emitter properties such as a high stability in oxygen, low resistivity and a low work function [18–20].

Physical vapour deposition has also been proven to be an effective way of producing highly crystalline IrO₂ thin films. Iridium was deposited on Ru(0001), covered with a single-crystalline RuO₂(110) layer. The iridium was oxidized either during deposition by a background oxygen pressure or during an annealing process in oxygen post deposition. The high quality in crystallinity was successfully proven using STM [21]. Using these thin films, the corrosion process of IrO₂(110)-based model electrodes in acidic environment was investigated. The promising results showed that even at high electrode potentials, the ultra-thin IrO₂ layers showed an unexpected stability [22].

As an alternative to the various deposition methods, it has been shown that an IrO₂ phase can be grown directly by oxidizing a metallic Ir substrate [23,24]. An IrO₂(110) structure was

successfully prepared by oxidizing an Ir(100) surface. The resulting surface proved to be effective for C-H bond breaking and allowed for efficient low-temperature activation of methane [25].

Few atomic-scale studies on IrO₂ single crystals exist. This is mainly because of the lack of commercial availability and difficulty to sputter and anneal IrO₂ in an ultra-high vacuum environment without severely reducing it.

Successful cross-sectional STM studies have been conducted on single crystalline IrO₂. By cleaving crystals *in situ* in an UHV environment, multiple surface facets such as the (110), (120), (130) and $\approx(89-1)$ were investigated, proving XSTM a viable technique to study oxide surfaces which are otherwise difficult to prepare [26].

The experimental surface science investigations are accompanied by theoretical calculations. There, IrO₂ is often compared with similar rutile oxides such as TiO₂, RuO₂ and SnO₂. DFT calculations on binary rutile MO₂ compounds yield values for the surface free energies of the different low-index facets [27]. Like TiO₂, the lowest surface energy corresponds to the (110) facet, whereas the largest surface energy corresponds to the (001) facet. The surface energies of the (101) and the (100) facet lie in between, with the (101) having a lower energy than the (100) [28]. Likely because the (111) facet is not stable on rutile TiO₂ it was not considered in the calculations. It should also be noted that these calculations deal with bulk truncated surfaces without consideration of possible surface reconstructions. Figure 1 shows a Wulff constructed equilibrium shape for rutile IrO₂.

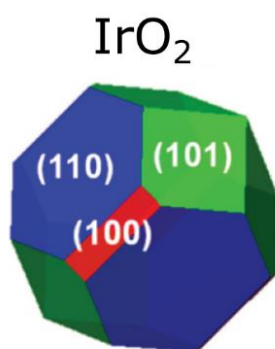


Figure 1: Wulff construction for IrO₂. Modified with kind permission from [27]. The facets show the following distribution according to their surface free energy: (110)-74 %; (011)-23 %; (001)-3 % [29]

4.2 Sample

The sample used for the measurements is a single crystal, grown by Prof. Zhiqiang Mao at Penn State University.

A crucible with IrO₂ is placed at the high-temperature (1250 °C) end of a tube furnace. Oxygen gas flow (100 ml/min) transports the chemical vapour to a quartz tube located near the colder

end of the furnace (1000 °C) where it condenses and forms a single crystalline structure. This growth process results in relatively small single crystals. The IrO_2 crystal used in this work was a flake measuring $\approx 2 \times 1 \times 0.1 \text{ mm}^3$. It was carefully mounted on a molybdenum sample plate using a piece of gold foil to ensure better thermal contact with the plate and spot-welded NiCrFe wires to hold it in place (Figure 2b). Figure 2a shows a SEM image of the mounted sample. Looking at the side of the sample reveals its thinness (Figure 2c).

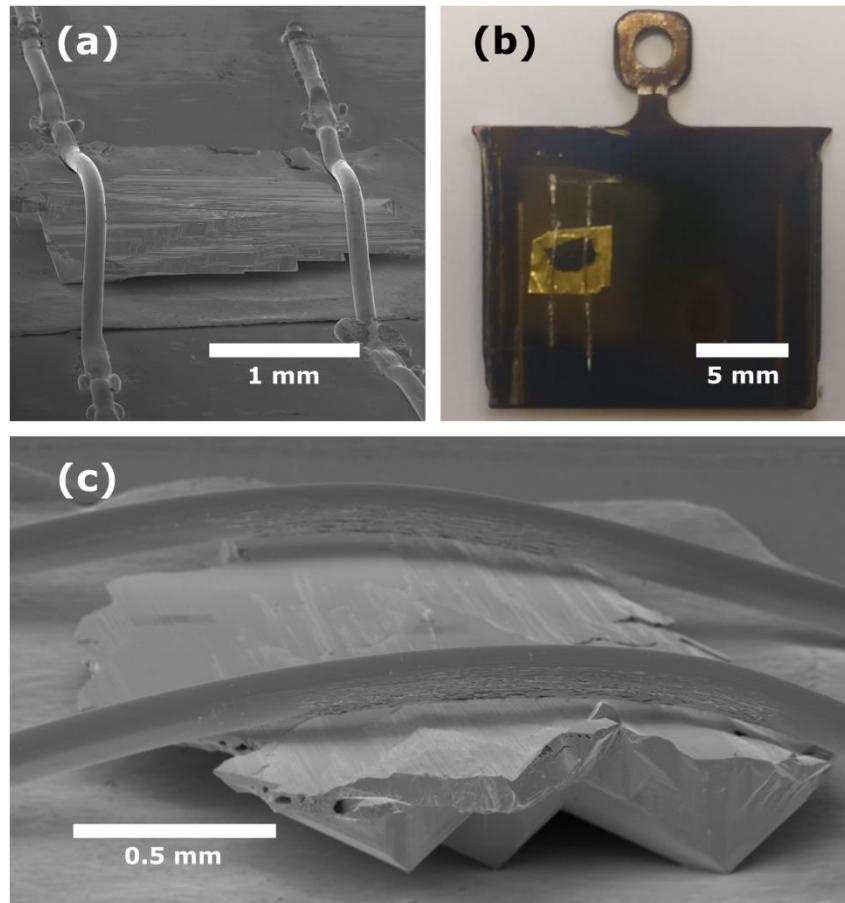


Figure 2: Images of the iridium oxide sample. (a): Scanning tunnel microscope image of the sample, held in place by spot-welded wires. (b): Image of the sample plate with the mounted single crystal. A gold foil was placed underneath for better thermal contact. (c): A side view of the sample (SEM) reveals the thinness of the single crystal.

For the preparation of the surface, the sample was sputtered with 1 kV Ar^+ for 5 minutes ($p_{\text{Ar}} = 8 \times 10^{-6} \text{ mbar}$, $I = 2 \mu\text{A}$) and subsequently annealed. As IrO_2 is easily reduced when heated in a vacuum environment, a relatively high oxygen background pressure is required to maintain the oxide phase. Figure 3 shows a phase diagram of IrO_2 and the metallic Ir phase [30]. With the help of an “oxygen shower” – a contraption that allows to move the oxygen inlet very close to the sample surface – an oxygen pressure of $> 5 \times 10^{-5} \text{ mbar}$ was achieved at the sample surface while maintaining a chamber background pressure of

5×10^{-6} mbar. A thermocouple readout temperature of 450 °C was chosen for the annealing process to avoid a reduction under these conditions.

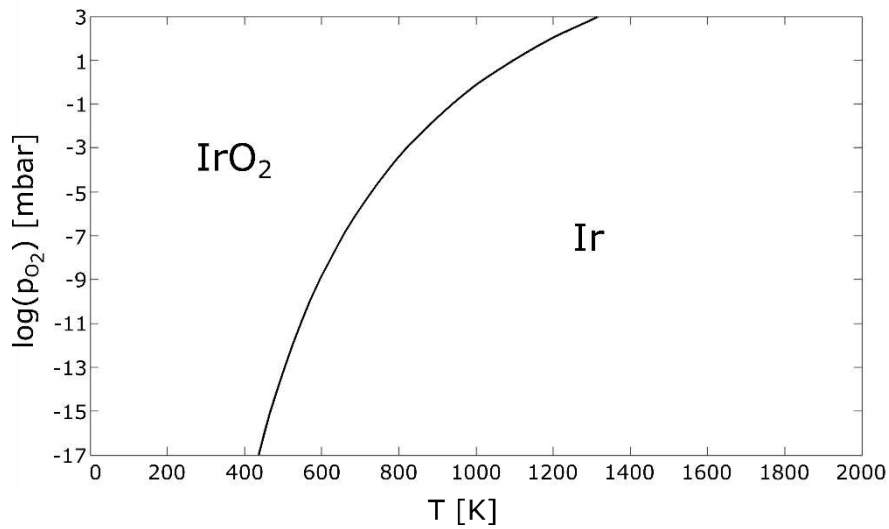


Figure 3: Phase diagram of iridium oxide depending on the partial oxygen pressure. As iridium oxide is easily reduced in UHV conditions, the oxygen pressure has to be chosen carefully during an annealing process. [30]

4.3 Results

4.3.1 XPS data

The small size of the sample made it impossible to eliminate contributions from the sample plate or the mounting wires. Because of this, the oxygen 1s peak does not give reliable information about the sample because the whole sample plate is oxidized in the annealing process. Therefore, only the iridium signal was investigated as it certainly had originated only from the sample. The Ir 4f peak shows a relatively high intensity compared to other Ir peaks such as the Ir 3d and the region does not overlap with any other elements which are present in the measurement, allowing for clean data analysis. A clear separation of the 4f 7/2 and the 4f 5/2 can be observed, resulting in two peaks which are positioned 3 eV apart.

Figure 4 shows an XPS data comparison of the Ir 4f region. One spectrum was acquired directly after the sample was sputtered for 10 minutes, while the two other spectra were obtained after annealing in O₂ at different temperatures (40 min, $p_{\text{O}_2} > 5 \times 10^{-5}$ mbar).

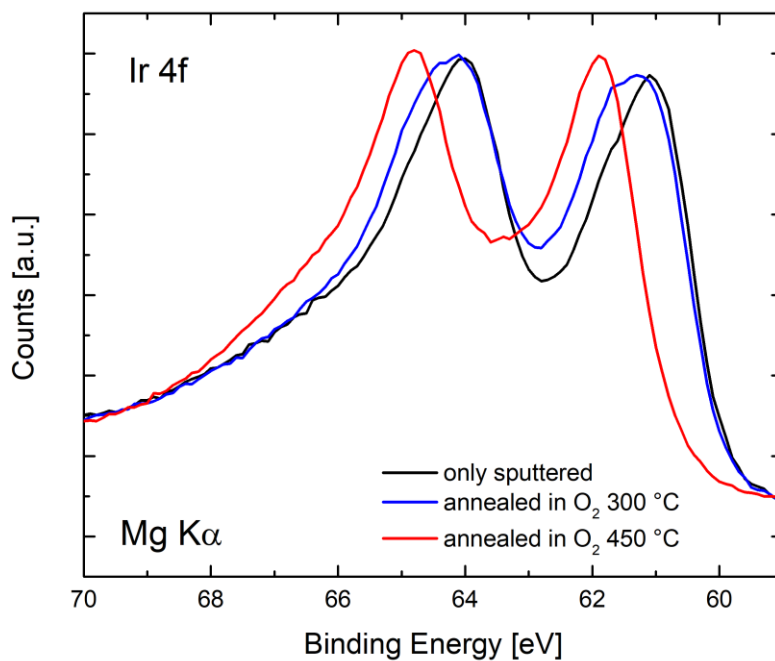


Figure 4: XPS spectra of the Ir 4f region (Mg anode, 15° emission). After annealing in oxygen (40 min, $p_{\text{O}_2} > 5 \times 10^{-5}$ mbar), the peaks shift to higher binding energies. The blue spectrum – measured after annealing in oxygen at 300 °C – is shifted less than the red spectrum and shows features resembling a double peak. After annealing at 450 °C the peaks are shifted by ≈ 0.8 eV in respect to the peaks recorded without annealing the sample (black spectrum).

The peak position of the sample annealed at 450 °C is shifted by ≈ 0.8 eV within respect to that of the sputtered sample. For the sample annealed at 300 °C the broad peak shapes together with the small double peak feature towards higher binding energies, suggest a multiple component peak.

The complex electronic structure of IrO₂ poses a challenge in determining the chemical state of surface species [31]. Using Functional Lorentzian (LF) and Gaussian-Lorentzian (GL) line shapes together with a Shirley background, a peak fit of the measured data is attempted using the program “Casa XPS (version 2.3)”. Fitting parameters found in literature [32] were applied. The unusual asymmetric core-electron line shapes of IrO₂ stem from a many-body screening response of the 5d conduction electrons [33].

Each Ir 4f peak can be broken down into three components: a metallic Ir peak, an IrO₂ oxide peak and a satellite feature from the oxide peak. While the Ir 5p 1/2 peak is also found in this region, its contribution to the Ir 4f spectrum is small (estimated to be under 5 % [31]) and was thus neglected. This results in a total of 6 peaks for fitting the Ir 4f region. The 4f 7/2 and 4f 5/2 are separated by an energy difference of 3 eV and the peak area of the 4f 5/2 peak is constrained to 0.75 times the area of the 4f 7/2 peak. Furthermore, the position and area of the IrO₂ satellite peaks was linked to the position and area of the main peaks (15.5 % and 11.6 % respectively, with an offset of 1.3 eV). The main peak positions were left unrestricted for the fitting process. The position of the low binding energy peak (red) shifts from ≈ 60.9 eV after sputtering (consistent with metallic Ir) to ≈ 61.3 eV after annealing at 450 eV. The oxide peak (blue) also shifts to higher binding energies during annealing. This results in a reduced difference in position between the metallic and the oxide peak after annealing at 450 °C (≈ 0.6 eV) when compared to the difference on the sputtered surface (≈ 0.8 eV). Table 1 shows a summary of the peak positions and areas for the 4f 7/2 peaks, and Figure 5 shows the fitted XPS spectra. While the metallic Ir peak is dominant with the sputtered sample, the sample annealed at 300 °C shows a slightly higher oxide peak and for the sample annealed at 450 °C, the area of the oxide peak is much (3.7 times) larger than the one of the lower binding energy peak.

	Ir 4f 7/2		IrO ₂ 4f 7/2		Δ position [eV]	area ratio
	position [eV]	area [% of total area]	position [eV]	area [% of total area]		
only sputtered	60.86	57.42	61.68	42.58	0.82	0.74
annealed 300 °C	60.94	56.87	61.77	43.13	0.83	0.76
annealed 450 °C	61.28	21.29	61.86	78.71	0.58	3.70

Table 1: Peak positions and areas for the iridium 4f 7/2 peaks according to an XPS peak fitting procedure. The spectra can be found in Figure 5. After annealing at 450 °C the area of the oxide peak is 3.7 times larger than the area of the metal peak. While both the metal peak and the oxide peak shift to higher binding energies during the annealing process, the shift is more noticeable for the metal peak.

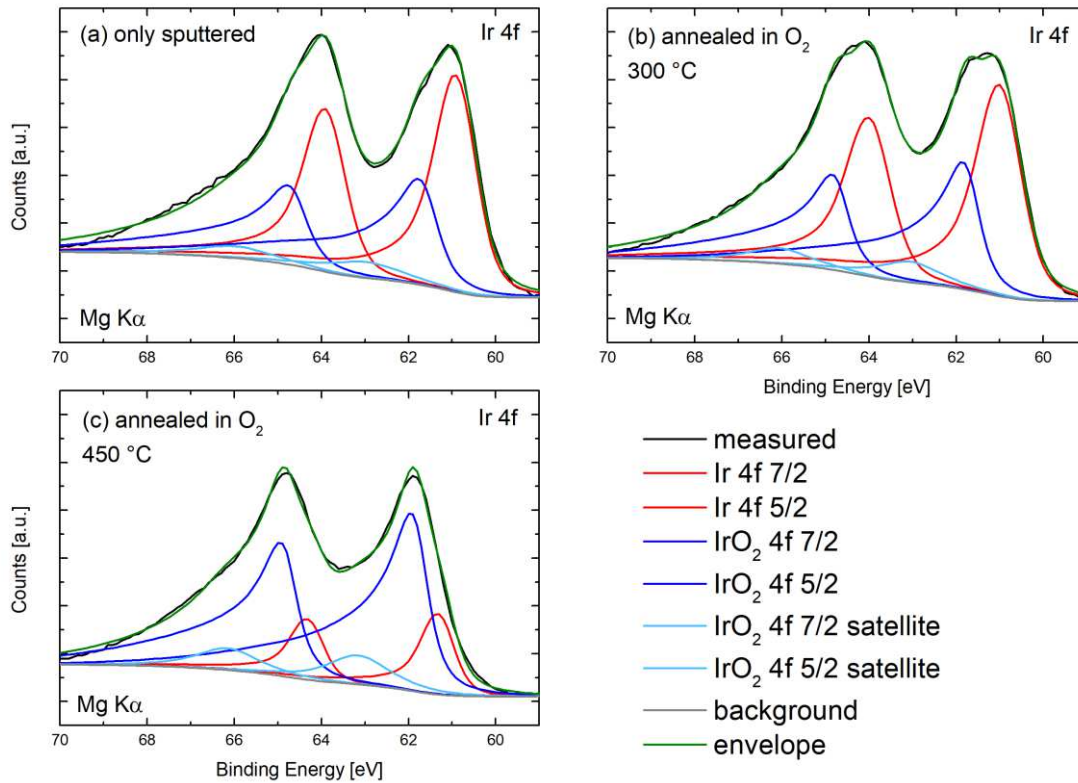


Figure 5: XPS spectra of the Ir 4f region with peak fits (Mg anode, 15° emission). Each of the two 4f peaks of iridium (7/2 and 5/2) can be fitted with three peaks: A metallic iridium peak and an iridium oxide peak that comes with a satellite feature. After annealing the sample in oxygen (40 min, $p_{O_2} > 5 \times 10^{-5}$ mbar) the area of the oxide peak is significantly higher than before the annealing process.

4.3.2 AFM data

The sample surface was probed with a commercial ambient pressure AFM setup (Agilent Technologies) using tapping mode. Figure 6 shows a typical obtained image ($10 \times 10 \mu\text{m}^2$). As already visible optically, the sample surface is highly faceted. A height profile was extracted from the AFM data (red line in Figure 6) and reveals a height difference of up to 400 nm. The measured angle between facets deviated drastically between individual measurements and was therefore deemed unreliable. The angular deviation could be explained by an inconsistent x/y calibration or an influence of the background subtraction process of the measurement software.

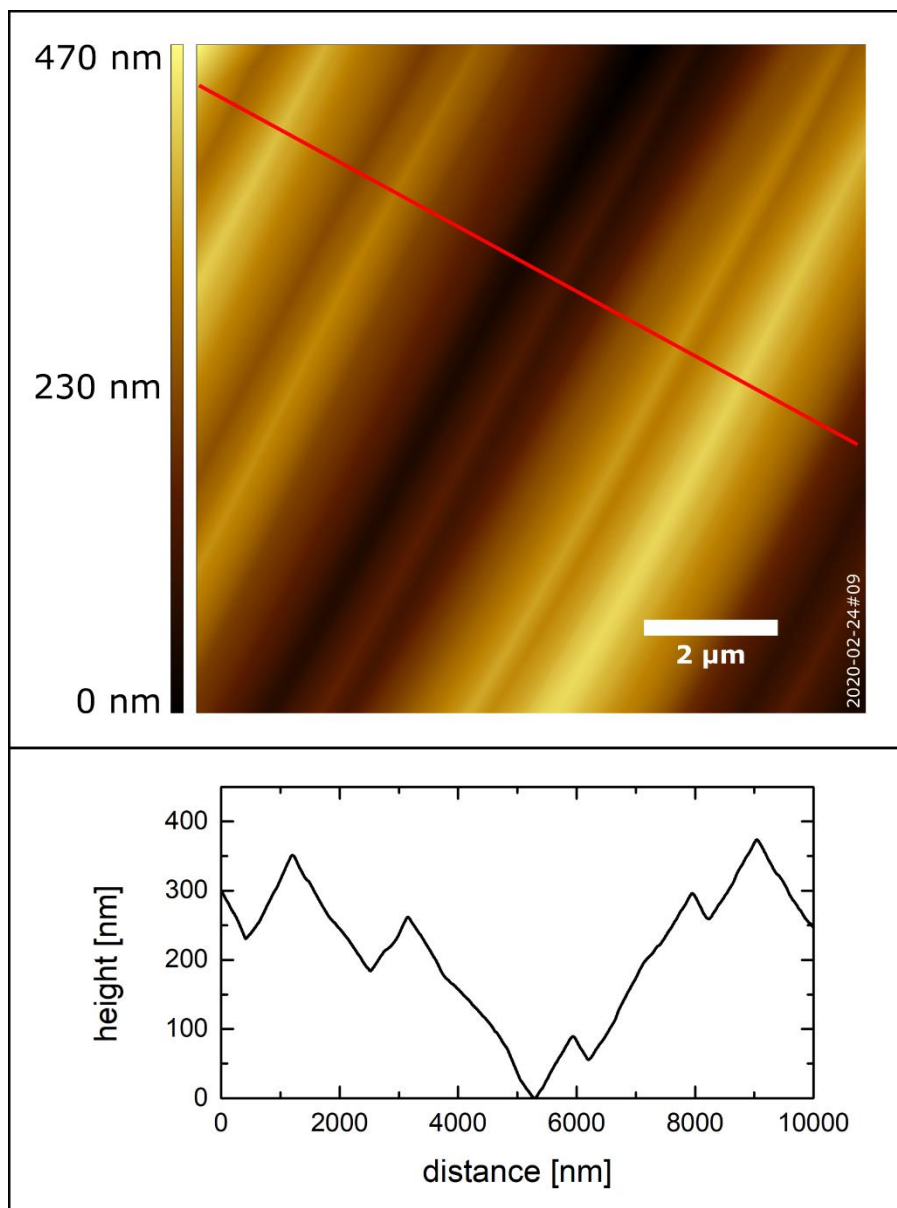


Figure 6: AFM image (tapping mode, topography, $10 \times 10 \mu\text{m}^2$) of the sample surface. A line profile was extracted from the image (red line) and is shown separately. The surface shows many facets with height differences of up to 400 nm.

4.3.3 EBSD data

Figure 7 shows recorded EBSD data of the sample surface. For three different regions, the detector intensity (greyscale images) and a colorized version – where the different colours represent the measured Euler angles – are shown. The image series decreases in size from left to right, (a) shows a region of $1200 \times 637 \mu\text{m}^2$, (b) shows a region of $66 \times 52 \mu\text{m}^2$ and (c) shows a region of $30 \times 23 \mu\text{m}^2$. The Euler angles were averaged within each coloured segment and Miller indices that represent the surface direction were calculated for each respective region (equation 4.1-4.3). Only regions with a low standard deviation of the two Euler angles necessary for the calculation were selected. Because of this, regions such as the red parts embedded in the larger green region in Figure 7c were neglected. The poor signal probably stems from the extreme angle under which some facets had to be measured.

Finally, the absolute angular difference to the next (101) equivalent plane was calculated and generally found to be between $\approx 2^\circ$ and $\approx 5^\circ$.

Table 2 shows a summary of the results for the images presented in Figure 7.

$$h = n \sin \Phi \sin \varphi_2 \quad (4.1)$$

$$k = n \sin \Phi \cos \varphi_2 \quad (4.2)$$

$$l = n \cos \Phi \quad (4.3)$$

h,k,l... Miller indices
 Φ, φ_2 ... Euler angles (Bunge's notation)
 n... arbitrary factor to make integer indices

The measurements reveal a vicinal surface in the (101) direction. The angular difference to the next (101) equivalent facet is small and generally $< 5.5^\circ$. This suggests large regions of (101) equivalent surface terminations on the crystal.

While it is possible that not all available crystal facets were imaged properly in the EBSD scans, as both the mounting wires and the highly faceted surface complicate the measurement process, the sample was scanned under multiple different detector angles to get a clear signal from as many regions as possible. Despite this effort, no facets showing any other direction than the (101) vicinal ones were detected.

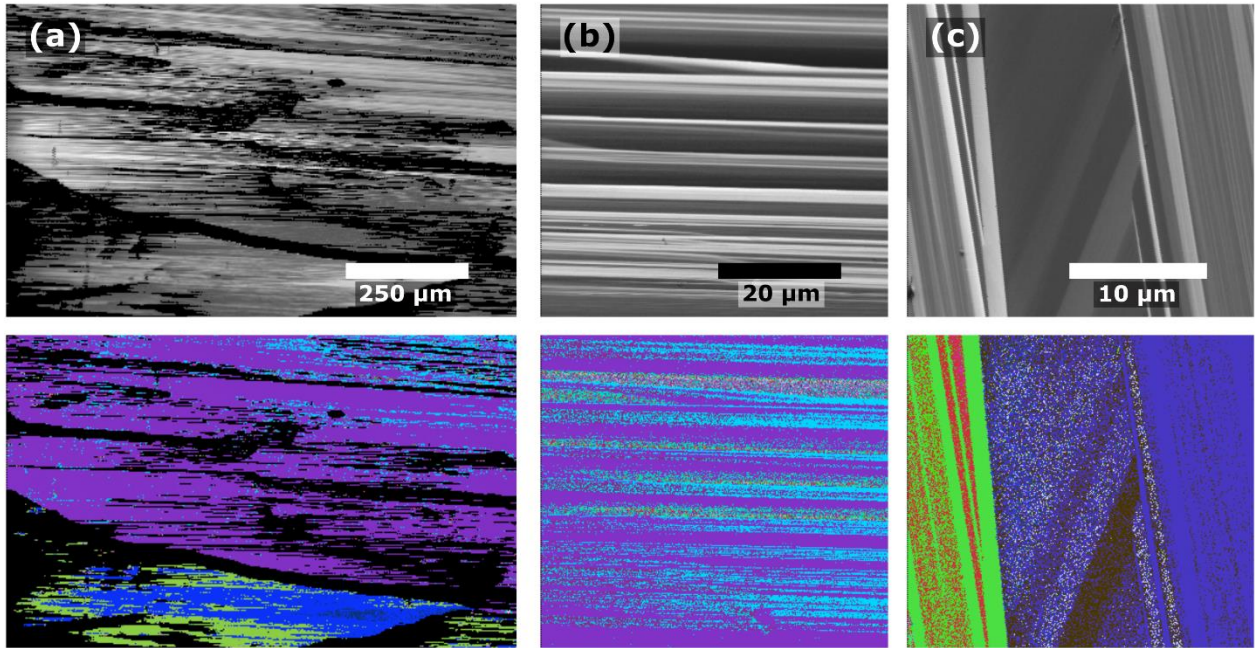


Figure 7: EBSD data of three different regions on the sample surface. The greyscale images each show the SEM detector intensity and provide real space images of three different sizes (a: $1200 \times 637 \mu\text{m}^2$, b: $66 \times 52 \mu\text{m}^2$, c: $30 \times 23 \mu\text{m}^2$). The colored versions represent the Euler angle distribution across the same region. Within each colour segment, the necessary Euler angles were averaged and processed to gain information about the angular deviation to the next $\{101\}$ equivalent plane.








Image	colour	relative area [%]	Φ [deg]	φ_2 [deg]	StdDev Φ [deg]	StdDev φ_2 [deg]	h	k	l	closest $\{101\}$ plane	Δ to $\{101\}$ [deg]
a		69.3	34.9	278.2	0.8	0.7	-7.0	1.0	7.1	$(\bar{1}01)$	4.7
a		9.9	35.7	350.9	1.8	0.3	-1.0	6.3	6.2	(011)	5.3
a		8.5	144.4	98.6	2.3	0.5	6.6	-1.0	-6.6	$(10\bar{1})$	5.0
b		44.8	34.6	278.1	0.2	0.5	-7.0	1.0	7.2	$(\bar{1}01)$	4.6
b		21.2	144.9	350.8	1.7	0.4	-1.0	6.2	-6.3	$(01\bar{1})$	5.3
c		15.0	146.1	94.4	3.9	1.1	13.0	-1.0	-13.6	$(10\bar{1})$	2.7
c		27.3	36.3	272.9	0.2	0.7	-19.8	1.0	18.9	$(\bar{1}01)$	2.1

Table 2: EBSD measurement data, the according images are presented in Figure 7. Only regions with a low standard deviation of the two respective Euler angles (Φ and φ_2) were selected for the calculations. The red region in image (c) is an example of a region with a poor signal and is therefore not shown in the table. The angular difference to the next $\{101\}$ equivalent facet is small and generally $< 5.5^\circ$.

4.3.4 STM data

STM images of the clean surface were acquired to ascertain the atomic-scale structure. Because the surface is heavily faceted, large scans with dimensions of $500 \times 300 \text{ nm}^2$ were initially taken to determine suitable terraces for images with a smaller scan size.

Figure 8 shows such large-scale images of the surface together with extracted line profiles. Already these overview scans reveal two different terrace structures. While some facets show rectangular-shaped terraces (Figure 8a), others have a more triangular shape (Figure 8b). The images are centred around the edge between two facets. The angle between the facets cannot be accurately measured in STM. Not enough scans were taken to make statistically accurate statements about the measured angles or on the absolute frequency of the two terrace structures. In the preliminary studies, there did not seem to be a clear correlation between the terrace shape and the measured location on the crystal. Coarse motion steps of the STM, which are in the range of micrometres, often led to measurements of both surface structures during the same scanning session.

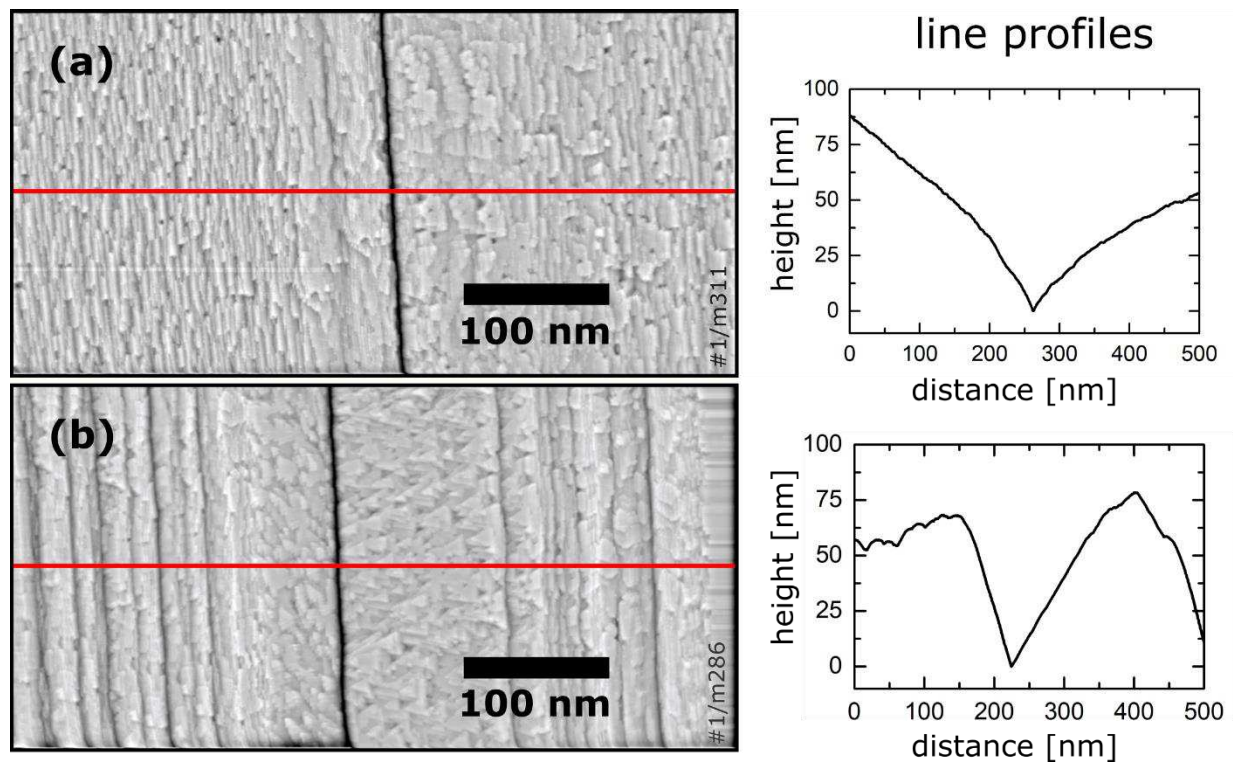


Figure 8: Large overview STM images of the surface with line scans, extracted from the center of the image (red lines) ($500 \times 300 \text{ nm}^2$, high-pass filtered, a: $U = -3.85 \text{ V}$, $I = 0.1 \text{ nA}$, b: $U = -3.85 \text{ V}$, $I = 0.1 \text{ nA}$). While image (a) shows terraces with a rectangular shape, image (b) shows triangular terraces. No region was found where one facet clearly showed the triangular terraces and the other exclusively the rectangular ones.

Smaller scale images ($100 \times 100 \text{ nm}^2$) already reveal some substructure on the terraces (Figure 9). These images are taken from the same region as Figure 8. While Figure 9a shows some

triangular looking terraces in the centre of the image, smaller scans of the region were not able to reveal anything but the surface structure of the rectangular terraces. More data is required to discern if all regions show the same terrace structure on both sides of the crevasse

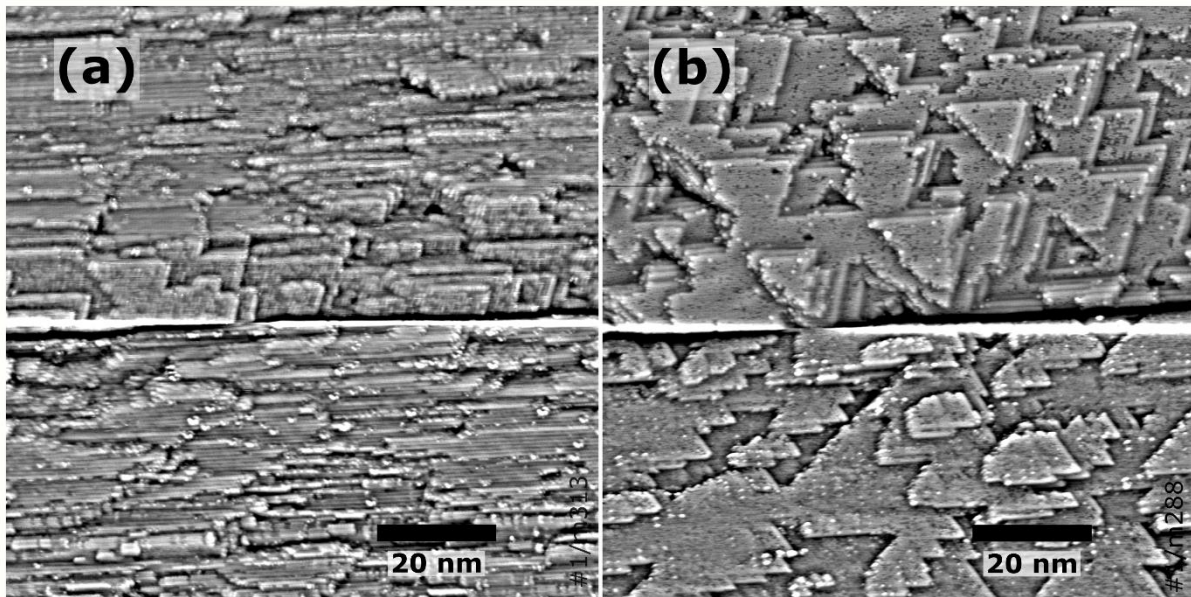


Figure 9: STM images ($100 \times 100 \text{ nm}^2$, high-pass filtered, a: $U = -2.8 \text{ V}$, $I = 0.1 \text{ nA}$, b: $U = -2.9 \text{ V}$, $I = 0.1 \text{ nA}$) show two different surface structures. Image (a) shows mainly rectangular terraces while image (b) shows triangular terraces. Some atomic substructure can already be seen on the terraces.

To achieve atomic resolution the scan size was decreased even further. Figure 10 shows a close-up look of individual rectangular terraces. These terraces have a length of about 15-40 nm and a width of about 5-8 nm. The images show an atomic structure with a rectangular unit cell. Some larger protrusions on the surface are clearly an image of the STM tip and measure $\approx 300 \text{ pm}$ in height (marked in blue). This suggests the existence of larger protrusions but does not allow to make precise statements about their shape.

Several small bright protrusions are present on the surface (marked with red arrows) which did not move around between subsequent scans at room temperature and have a height of $\approx 50 \text{ pm}$. These protrusions seem to be ordered along the underlying rows and always appear in pairs in Figure 10. This is likely an effect of a double tip as other images of the rectangular terraces (Figure 11) show single protrusions of the same size, ordered along the underlying rows. Figure 11 also shows tip-artefacts which also measure $\approx 300 \text{ pm}$ in height and are marked in blue. Additionally, the different contrast in the image makes a slight zig-zag pattern along the lines visible (marked in yellow).

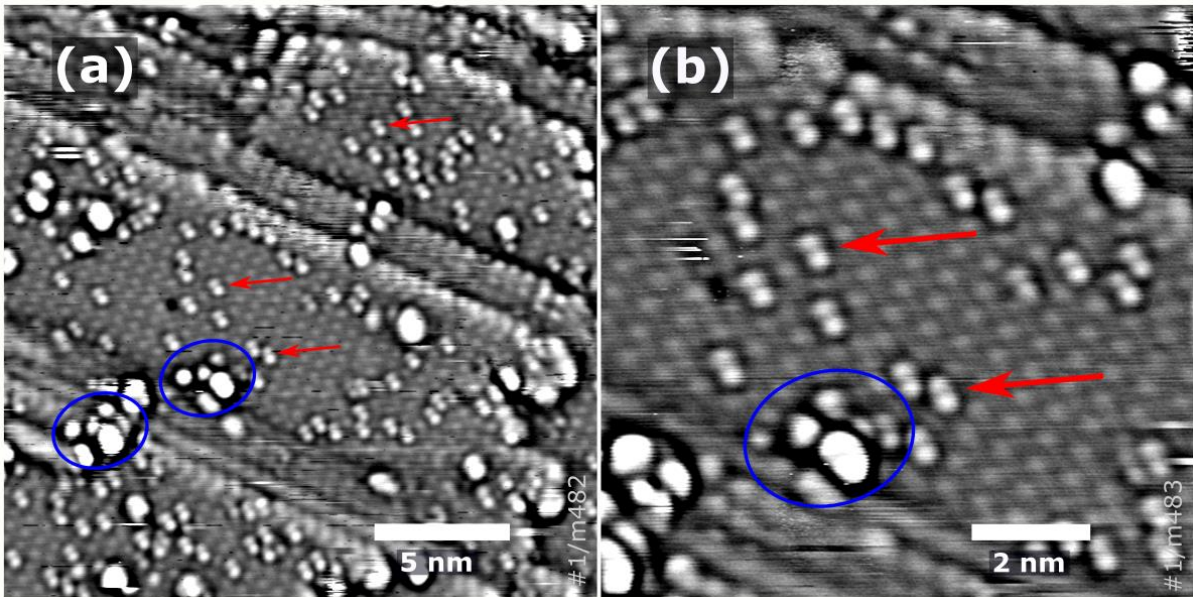


Figure 10: STM images with atomic resolution of the rectangular shaped terraces (a: $22 \times 22 \text{ nm}^2$, high-pass filtered, $U = -2 \text{ V}$, $I = 0.1 \text{ nA}$; b: $10 \times 10 \text{ nm}^2$, high-pass filtered, $U = -2 \text{ V}$, $I = 0.1 \text{ nA}$). The small protrusions (red arrows) measure $\approx 50 \text{ pm}$ in height, seem to be ordered along the underlying rows and did not change position in between scans at room temperature. They appear in pairs, likely due to a double tip. Larger protrusions (blue) imaged the STM tip and measured $\approx 300 \text{ pm}$ in height.

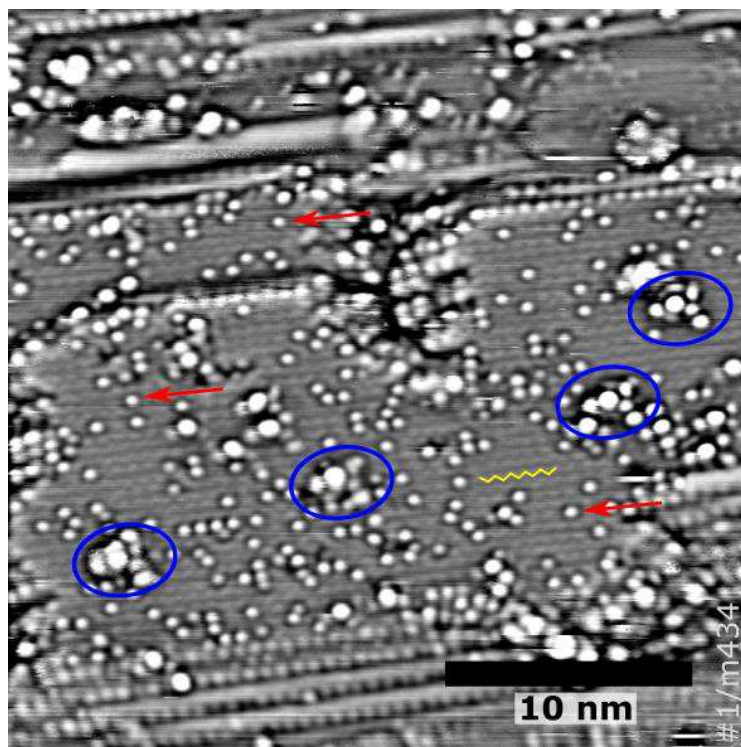


Figure 11: STM image of the rectangular terraces ($30 \times 30 \text{ nm}^2$, high-pass filtered, $U = -2 \text{ V}$, $I = 0.2 \text{ nA}$). This image shows a different region and has a different contrast than Figure 10. The small protrusions (red arrows) measure $\approx 50 \text{ pm}$ in height and seem to be ordered along the underlying rows. The large protrusions (blue) imaged the STM tip and measured $\approx 300 \text{ pm}$ in height. A zig-zag pattern of the underlying rows is visible and is highlighted in yellow.

STM images of the triangular shaped terraces reveal an atomic structure with a slanted quadrilateral unit cell (Figure 12). It is not clear whether the atomic structure show a rhombic or hexagonal unit cell as the angular difference lies within the error margin of the STM. There are fewer protrusions than on the rectangular terraces and they seem to appear non-periodically. Figure 12 shows multiple images of the STM tip which suggests the presence some protrusions on the surface. These protrusions measure ≈ 10 pm in height and are marked in blue.

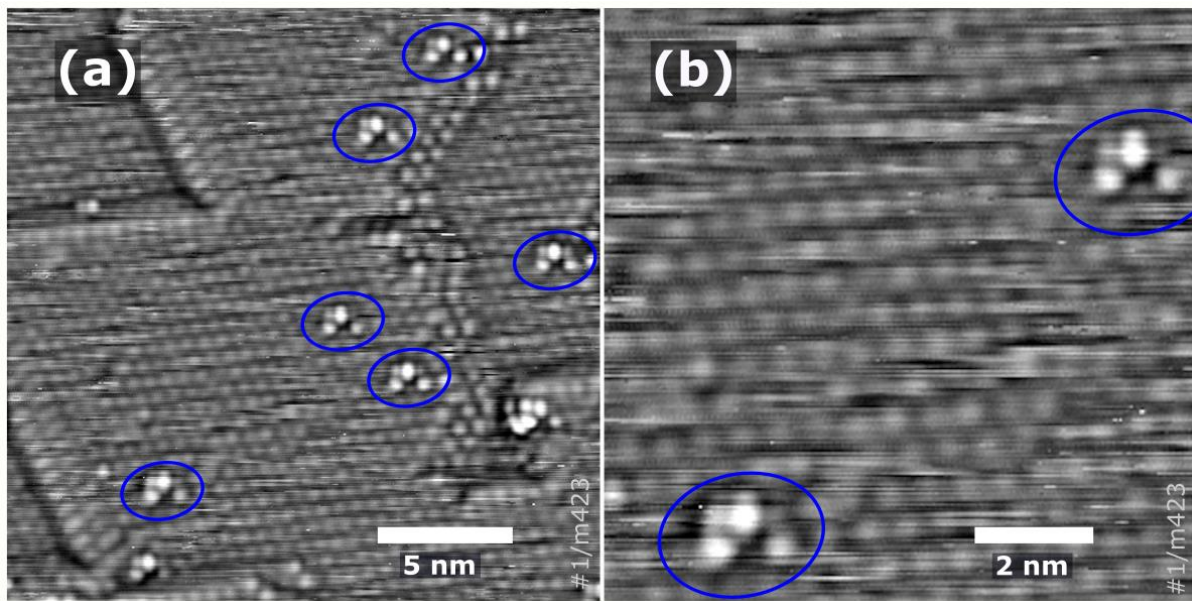


Figure 12: STM images with atomic resolution of the triangular shaped terraces (a: 22×22 nm², high-pass filtered, $U = 2$ V, $I = 0.1$ nA; b: 10×10 nm², high-pass filtered, $U = 2$ V, $I = 0.1$ nA). Few protrusions can be seen on the surface. The visible protrusions (marked in blue) measure ≈ 10 pm in height and show the exact same shape, strongly indicating an imaging process of the STM tip on surface protrusions (“tip artefacts”).

For accurate measurements of lattice parameters, the STM images were corrected for distortion and creep of the piezo scanner as described in ref. [34]. After correcting for nonlinear distortion, caused by the piezo creep, corrections for linear distortion were performed. These corrections usually are based upon prior knowledge about a periodic structure on the surface. As the surface structures were entirely unknown, reference measurements on a known surface (Rh(111)) were done to correct for the intrinsic x/y discrepancy of the STM scanner. The difficulty to perform corrections for a potential shear of the images means that the portrayed angles have an uncertainty to them.

Once the images were corrected in this manner, individual protrusions of the surface lattice were localized using a feature recognition procedure. A point map was generated, and the lattice distances were measured using an FFT and a grid measurement procedure.

4.4 Discussion

Both STM and EBSD data suggest the presence of a (101) surface termination on the sample. That claim is strengthened by the fact that the $\text{IrO}_2(101)$ termination is one of the most stable ones as predicted by calculations [27–29] and has previously been reported to form on single crystal platelets grown by a chemical vapor transport technique, as confirmed by X-ray diffractometry [26].

On grown thin films, the substrate type and orientation heavily influence the growth direction. Yet even when not trying to purposefully engineer a crystalline (101) structure, many studies report the existence of a (101) contribution in XRD measurements, often as one of the most dominant facets [12–14,16,35].

Figure 13 shows a model of the bulk truncated $\text{IrO}_2(101)$ surface. The rectangular unit cell measures $0.55 \times 0.45 \text{ nm}^2$ which corresponds to recorded STM data on the rectangular terraces. Figure 14 shows an overlay of the (101) surface model with an acquired STM image. When comparing the image to theory, it is apparent that the atom in the centre of each unit cell is poorly visible in STM. Some images on the rectangular terraces though show a different contrast and reveal a zig zag pattern (Figure 14 red inset) which indicates the presence of the central atom.

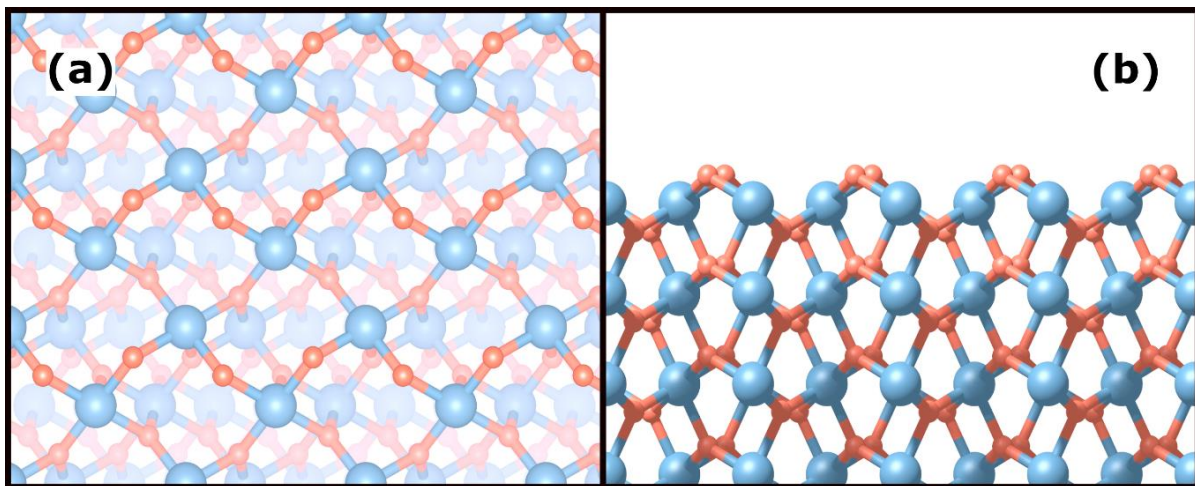


Figure 13: Model of the bulk truncated $\text{IrO}_2(101)$ surface. (a) shows a top view, (b) shows a side view of the crystal model. Iridium atoms are shown in blue, oxygen atoms in red.

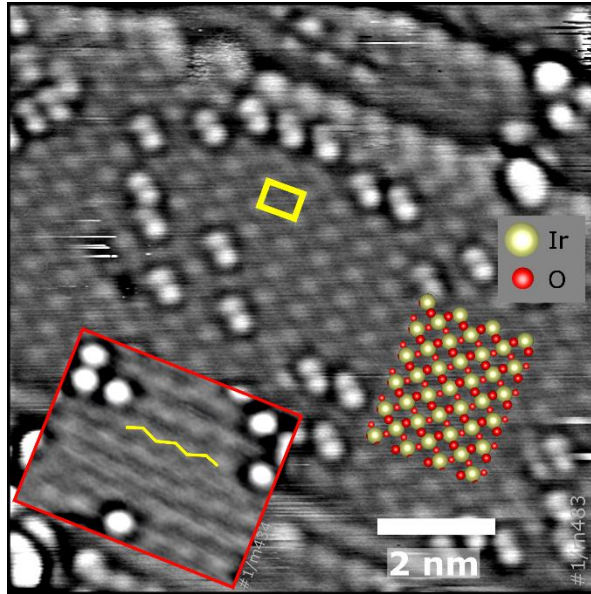


Figure 14: Comparison of the $\text{IrO}_2(101)$ surface model with recorded STM data ($10 \times 10 \text{ nm}^2$, $U = -2 \text{ V}$, $I = 0.1 \text{ nA}$). Iridium atoms are shown in gold, oxygen atoms in red. The measured distances of the unit cell match the bulk truncated model ($0.55 \times 0.45 \text{ nm}^2$). The red inset shows an image of the same surface termination, recorded with a different contrast. Here, the central atom is visible, resulting in a slight zig zag pattern on the image.

As for the surface structure with the seemingly hexagonal or rhombic unit cell that was visible in STM, the matter is not quite as clear. Measurements reveal unit cell dimensions of 0.55 nm in both directions. Since there are no reference structures in the same image, the angle between the unit cell sides cannot be measured accurately. Both an angle of 70.76° and an angle of 60° would fit the data and would result in a rhombic or a hexagonal unit cell respectively.

If a rhombic unit cell were assumed, the $\text{IrO}_2(111)$ termination would fit the STM data. Figure 15 shows a model of the bulk truncated $\text{IrO}_2(111)$ surface and Figure 16 shows an overlay of the bulk truncated (111) surface with an STM image. While the interatomic distances fit the recorded data quite nicely, EBSD measurements were not able to confirm a (111) orientation of the crystal. Additionally, the (111) surface termination of binary rutile MO_2 compounds such as TiO_2 , RuO_2 and IrO_2 is not even considered in most surface energies calculations as it is usually not stable [27].

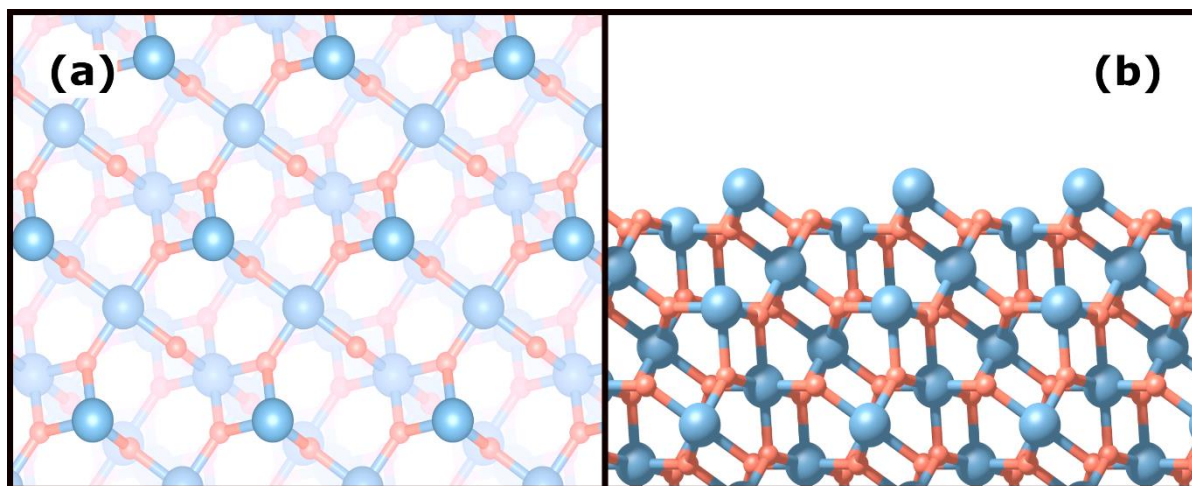


Figure 15: Model of the bulk truncated IrO₂(111) surface. (a) shows a top view, (b) shows a side view of the crystal model. Iridium atoms are shown in blue, oxygen atoms in red.

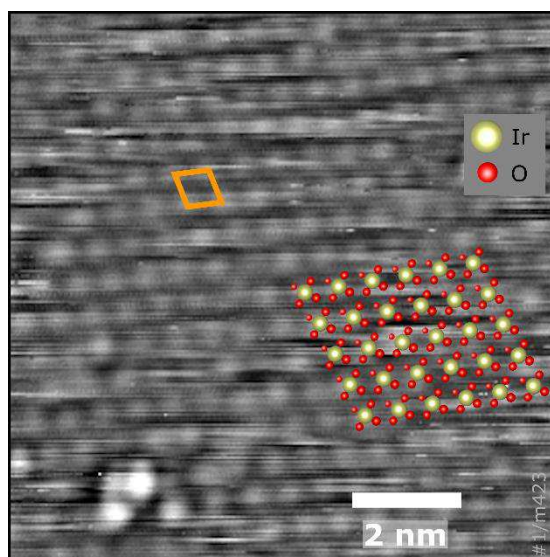


Figure 16: Comparison of the IrO₂(111) surface model with recorded STM data ($10 \times 10 \text{ nm}^2$, $U = 2 \text{ V}$, $I = 0.1 \text{ nA}$). Iridium atoms are shown in gold, oxygen atoms in red. The measured distances of the unit cell match the bulk truncated model ($0.55 \times 0.55 \text{ nm}^2$).

Recent calculations on structural evolution of IrO₂ nanoparticles in electrochemical conditions have shown that at an onset potential of 0.9 V the IrO₂(111) facet starts to emerge in the predicted Wulff shape [29]. For $U > 1.3 \text{ V}$ the calculated absolute surface free energy of the (111) termination is the lowest of all surface terminations, resulting in nanoparticles entirely formed of these (111) facets.

While these calculations still await experimental confirmation and the measurement conditions in this work certainly differ, it might be an indication that the IrO₂(111) facet should not be as easily disregarded as it has been in the past.

Alternatively, the observed structure could also have a hexagonal unit cell. A possible explanation for such a geometry could be an oxygen overlayer on the metallic Ir(111) phase.

LEED measurements in combination with dynamic calculations have shown that a $p(2\times 2)$ oxygen superstructure can form on a clean Ir(111) surface after exposure to oxygen at room temperature [36]. *Ab initio* calculations also agree that the $p(2\times 2)$ superstructure is a stable surface configuration [37]. Figure 17 shows a model of one of the proposed oxygen overlayers. More recent work provided STM images that confirm the existence of such an oxygen overlayer at certain oxygen coverages [38]. There the oxygen $p(2\times 2)$ overlayer was observed after exposure of the clean Ir(111) surface to 600 L molecular oxygen at 375 K. When more oxygen was available (750 L at 375 K), a $p(2\times 1)$ structure was observed.

During the annealing process depicted in this thesis, more than 600 L oxygen is available, still it is unclear how comparable these coverages are, since the oxygen deposition process in this work was done at higher temperatures ($450\text{ }^\circ\text{C} \approx 750\text{ K}$).

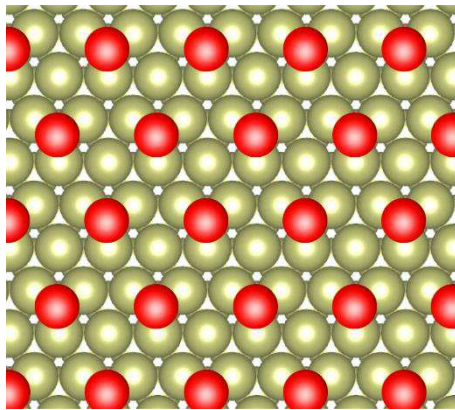


Figure 17: Model of the iridium (111) surface with a $p(2\times 2)$ oxygen superstructure on top. Iridium atoms are shown in gold, oxygen atoms in red. The distance between the hexagonally ordered oxygen atoms (0.55 nm) would fit the recorded STM data.

Looking at XPS data, the Ir 4f region always contains a contribution of a lower energy peak even after annealing in oxygen. This could be an indication of the presence of a metallic phase at the surface. The Ir(111) facet is – contrary to the $\text{IrO}_2(111)$ facet – the most stable termination. Given the difficulty of growing IrO_2 crystals, it is possible that there is some amount of metallic iridium left on the sample. Also, after sputtering, a higher metallic contribution was observed in XPS. It is possible that some of the Ir atoms reconstruct to metallic Ir(111) before they can be reoxidized in the annealing process.

The whole “hexagonal-like” reconstruction could be induced by impurities. On the rutile TiO_2 (001) surface – which is equivalent to the (101) surface – such a “pseudo-hexagonal” structure has been previously observed. There, it has been related to a segregation of bulk impurities [39] or a purposeful deposition of metals, forming a mixed oxide monolayer [40–43].

Figure 18 shows an STM image of the clean TiO_2 (011) sample surface [44]. The “hexagonal-like” structure there was associated with the segregation of magnesium impurities from the crystal bulk. The segregation of magnesium was observed by low-energy ion scattering spectroscopy (LEIS) and confirmed by temperature dependent XPS measurements.

Similar to the presented results on TiO_2 , low-energy ion scattering spectroscopy (LEIS) measurements should be conducted on the IrO_2 sample surface to exclude the possibility of a contamination-induced reconstruction.

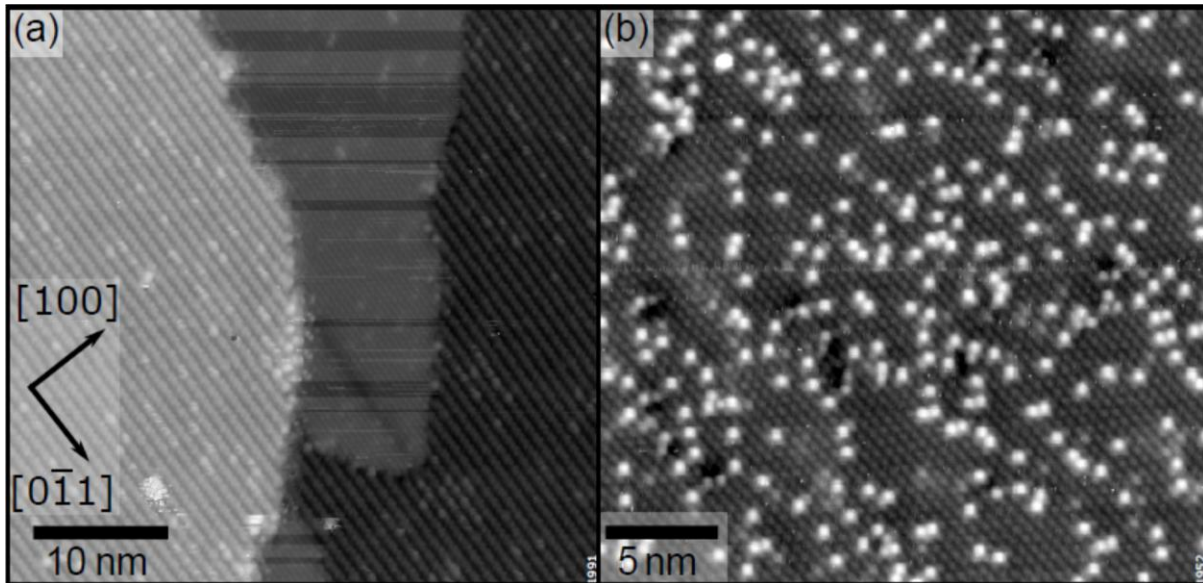


Figure 18: STM images of the reconstructed TiO_2 (011) surface. (a) shows large regions of the ‘usual’ (2×1) reconstructed surface with the quasi-hexagonal mixed Ti-Mg oxide phase in the middle of the terrace. (b) shows only the quasi-hexagonal surface. The bright protrusions on the surface are attributed to hydroxyl groups from the residual water in the UHV chamber. Image kindly provided by Jan Balajka [44].

4.5 Summary and Outlook

An iridium dioxide single crystal was investigated using surface science techniques such as AFM, STM, XPS and EBSD. Suitable sample preparation parameters were found to achieve a clean IrO₂ surface. Despite precautions to avoid a reduction, a metallic Ir phase always contributed to the XPS spectra. The amount of metallic iridium stayed constant throughout various preparation and measurement cycles, suggesting no accumulating reduction of the surface under the applied annealing conditions. On the strongly faceted surface, two different atomic surface reconstruction were imaged with STM. The reconstruction with a rectangular unit cell fits the IrO₂(101) surface. EBSD measurements confirm that the surface is a vicinal surface in a (101) direction with an angular deviation of $< 5^\circ$ for most measured facets.

The origin of the surface reconstruction with a rhombic or hexagonal unit cell is not quite as clear. Possibilities include the IrO₂(111) termination, an oxygen overlayer on metallic iridium or a contamination induced reconstruction.

All the measurements presented were conducted on one single sample, and it is crucial to grow and prepare multiple samples for a more in-depth study of the surface. As an addition to single crystals, thin films could also provide interesting reference data given the ability to grow them in a reliable and reproducible way with a specific orientation. Due to the similar interatomic distances and the same rutile structure, the TiO₂(101) surface might be a suitable candidate for such a thin film growth process.

This work aims to shed a light on the atomic surface structure of IrO₂ single crystals, yet many questions remain. Rather than providing a thorough analysis, the goal was to show that these crystals can be investigated on an atomic level using surface science techniques such as STM. The preliminary data presented in this work is a step towards a greater understanding of the versatile material iridium dioxide.

5. Hematite – $\alpha\text{-Fe}_2\text{O}_3$

5.1 Introduction and Motivation

Iron oxides play an important role in a wide array of scientific applications such as environmental chemistry, biomedicine, microelectronics and heterogeneous catalysis [45]. The abundance of iron oxides in the Earth's crust makes these materials appealing due to their availability and resulting affordability.

In an ambient environment, hematite ($\alpha\text{-Fe}_2\text{O}_3$; for simplicity of notation the “ α ” is dropped throughout this thesis) is the most stable form of iron oxide. It has a distinct red colour which is responsible for the typical colour of rust.

In the field of photoelectrochemistry, hematite is a material of high interest due to the band gap of ≈ 2.2 eV, which allows it to absorb visible light and due to its chemical stability in aqueous environments. In particular, it is a promising candidate for electrochemical water splitting ($2\text{H}_2\text{O} + 2\text{e}^- \rightarrow \text{H}_2 + 2\text{OH}^-$). The performance of hematite in this process is severely limited due to a low absorption coefficient [46] and the high electrochemical potential needed to initiate the water oxidation [47,48]. While these issues prevent the usage of pure hematite as a feasible photoanode material, introducing another material such as titanium as a dopant or iridium as an ultra-thin monolayer can dramatically increase photocatalytic activity [49,50].

Concerning single-atom catalysis on iron oxides, many studies have been conducted using (FeO_x) nanocrystallites as a support system. Using gold or platinum as single metal atoms, a high activity for CO oxidation and catalytic formaldehyde oxidation has been reported [51–54]. Iridium and palladium single atoms have been successfully used to increase the activity for the water gas shift reaction [55,56] and theoretical investigations aim to predict stability and activity of metal atoms on FeO_x surfaces [57,58].

Important insights have been gathered by using the model system of the magnetite (Fe_3O_4) (001) surface. The $(\sqrt{2} \times \sqrt{2})R45^\circ$ reconstruction of the surface provides ideal anchor points for single metal adatoms allowing for controlled studies of chemical processes using various surface science methods [59]. Unfortunately, the surface reconstruction is only stable in an UHV environment [60], rendering the material possibly unsuitable for actual application in ambient pressures unless adatoms are stabilized by ambient influences such as water.

The hematite surface on the other hand is stable in an ambient environment and thus could provide a much-needed support material for single atoms. Recently, iridium atoms dispersed on the hematite (001) surface have been shown to form dinuclear heterogeneous catalysts

which proved to have a high stability against detachment or aggregation and showed high activities toward H_2O photooxidation [61].

For all single atom catalysis applications, a deep understanding on an atomic level is required to tailor strong bonding sites needed to stabilize adatoms. This work presents a summary on the complication of measuring a poorly conducting material such as hematite in STM and shows preliminary work of surface defect generation and rhodium deposition on the hematite (012) (1×1) reconstruction.

5.2 Samples

For the experiments conducted in this work, four different hematite samples were used. One sample was a natural single crystal (SPL) while the other three were homoepitaxial thin films grown on hematite single crystals.

Pure hematite single crystals with little impurities have a very poor conductivity. This poses a challenge as some experimental techniques such as STM and LEED require a conductive surface. To achieve sufficient surface conductivity, a hematite single crystal has to be prepared in a specific way. Sputtering the sample surface leads to a preferential removal of oxygen. After several consecutive sputter and anneal cycles, the top layers will have a lower oxygen to iron ratio than before. This process – practically a reduction of the surface – results in an iron enriched surface region and thus leads to increased conductivity. To avoid a total reduction of the sample to magnetite (Fe_3O_4), the sample must be annealed in oxygen regularly to re-oxidize the outmost surface layers. If done correctly the result is a well-ordered hematite surface which is conductive due to an underlying reduced region with more iron interstitials and oxygen vacancies than in the usual Fe_2O_3 bulk. While this procedure has been proven to work with different hematite samples, it is not without problems. The many (60-100) sputter cycles roughen the surface significantly, which complicates the acquisition of atomically resolved STM data, as flat terraces become hard to find.

Usually, rough samples can be flattened by annealing at high temperatures. Annealing hematite samples at high temperatures requires a very high oxygen pressure to maintain the hematite phase. This oxygen would re-oxidize the subsurface region, undoing the progress made towards surface conductivity.

The hematite single crystal used in this work was treated accordingly to make it conductive. Over time even the sputtering processes used for normal sample cleaning routines lead to a roughening of the surface until the sample condition makes it very challenging to find flat terraces in STM. Growing a doped thin film is a way to sidestep the issues that come with the aforementioned preparation process. These grown thin films have a much flatter surface while still being conductive enough to measure in STM. Figure 19 shows a comparison of STM images ($200 \times 200 \text{ nm}^2$) of the undoped crystal and a titanium-doped thin film. While the surface of the undoped sample is very rough and dominated by steps and “mountain range”-like structures., the surface of the doped thin film shows large flat terraces.

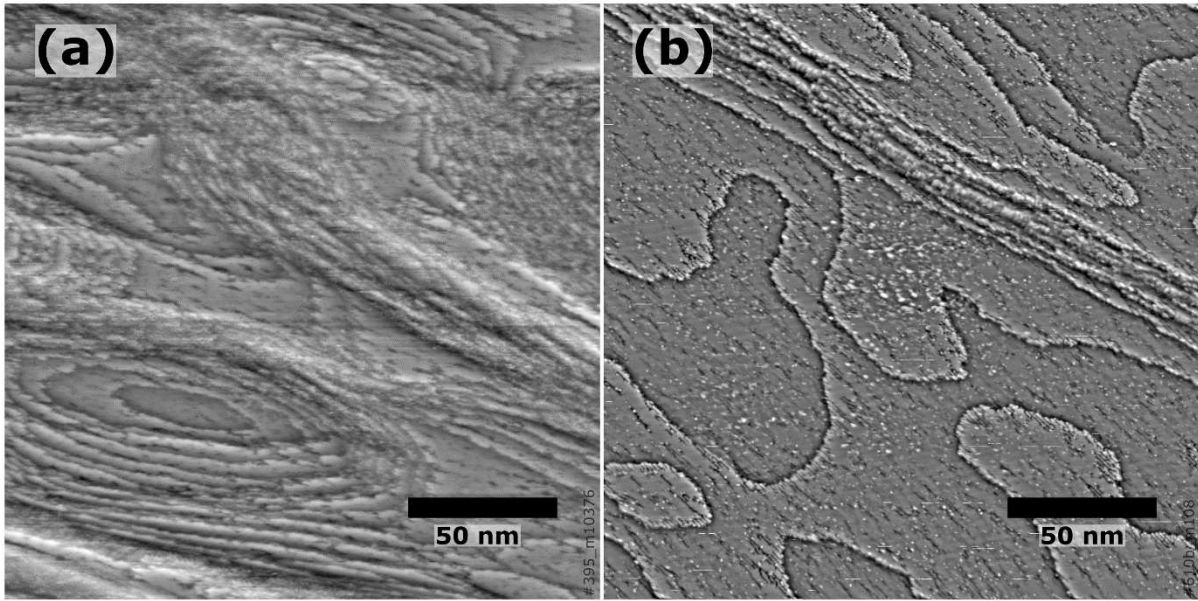


Figure 19: STM images of the clean $\text{Fe}_2\text{O}_3(012)$ (1×1) surface of the undoped (a) and 0.8 % Ti-doped thin film sample (b) ($200 \times 200 \text{ nm}^2$, high-pass filtered, a: $U = 3 \text{ V}$, $I = 0.1 \text{ nA}$; b: $U = 2.7 \text{ V}$, $I = 0.25 \text{ nA}$). The surface of the undoped crystal is dominated by steps, large terraces are few and far between. The Ti-doped sample shows a flatter surface structure with large terraces.

Using titanium as a dopant, even very low dopant-percentages (in the region of 0.01 at%) result in enough surface conductivity to perform STM and LEED measurements. Titanium has a strongly preferred oxidation state of +4. The iron atoms in hematite are all in the oxidation state of +3, hence, if a Ti atom substitutes a Fe atom, there is excess negative charge which leads to conductivity. Here only a simplified process description can be given, more detailed work on polaron hopping and the influence of dopants on conductivity can be found in literature [62]. More information about titanium doping of $\text{Fe}_2\text{O}_3(012)$ thin films can be found in ref. [63]. Three Ti-doped hematite thin films were used for this work. The Ti doping levels were 3.1 at%, 0.8 at% and 0.03 at% (below referred to as the “ultra-low Ti-doped sample”) respectively. The following section gives an overview of the growth process using the ultra-low Ti-doped sample as an example.

5.2.1 Growth process

All substrates used for thin film growth were hematite single crystals (SurfaceNet GmbH, one side polished, $< 0.3^\circ$ miscut). Two substrates had dimensions of $5 \times 5 \times 0.5 \text{ mm}^3$ while the third one measured $10 \times 10 \times 1 \text{ mm}^3$.

Prior to thin film deposition, a magnetron sputter source was used to coat the corners of the insulating substrates with platinum. This ensures electrical contact between the thin film and the sample plate. Details on this Pt deposition process can be found in literature [64].

All samples were grown in the same UHV chamber using pulsed laser deposition (PLD). The vacuum chamber is a complex system consisting of multiple connected parts, only the PLD setup will be described in more detail here. To grow multi-component thin films using PLD, usually multiple targets are used. For the film with higher doping levels (3.1 at%) and (0.8 at%) both a Fe_3O_4 and a TiO_2 single crystal were used as targets. The elemental composition can be controlled by alternating the number of pulses fired on each target. The deposition process is carried out in an oxygen background pressure (2×10^{-2} mbar) to ensure a sufficient oxidation and the sample is kept at a high temperature (850 °C) to assist diffusion of the deposited particles. This ideally results in a homogeneous doping level throughout all the deposited material.

In the following section, the generation of the ultra-low-doped $\text{Ti}:\text{Fe}_2\text{O}_3$ film is discussed. When significantly reducing the doping level, the time between the “shots” on the Ti target would become very large. This generates a problem as each Ti layer is buried between many hematite layers. It is possible that the diffusion processes would no longer be able to guarantee a stoichiometrically homogenous thin film. Because of this, a mixed $\text{Fe}_2\text{O}_3/\text{Ti}$ target was created.

To generate a target with a relative Fe/Ti atom ratio of 99:1, Fe_2O_3 and TiO_2 powders (Alfa Aesar) were carefully weighted, mixed and ground down in an agate mortar. A silicone mould was created using a Teflon mould, liquid silicone and a hardener. The mixed powder was inserted into the silicone mould, wrapped in protective layers of rubber and pressed inside an oil press. The proto target was then put into a platinum crucible and baked for 6 h in a furnace at 1200 °C (5 °C/min ramp up, 5 °C/min ramp down, 6 h at maximum temperature, ≈ 1 bar oxygen flow). To avoid any contamination of the target surface with Pt, the target was embedded into the same $\text{Fe}_2\text{O}_3/\text{TiO}_2$ -powder it consists of, preventing contact with the crucible walls. To achieve a flat target surface, the skewed target was cut with a diamond wire saw and polished with silicon carbide paper.

Using this already doped target in addition to the pure Fe_3O_4 crystal target, the ultra-low-doped hematite thin film was grown in the PLD chamber. Both targets were pre-ablated with laser pulses to avoid surface contaminations. An oxygen pressure of 2×10^{-2} mbar was maintained during the deposition process and the sample temperature was kept at 850 °C. For every 100 pulses on the magnetite target, 3 pulses were shot at the mixed $\text{Ti}:\text{Fe}_2\text{O}_3$ target (laser settings: 2 J/cm², 5 Hz). 600 such deposition cycles were done resulting in a thin film with a nominal Ti doping percentage of 0.03 at%.

5.2.2 Sample preparation

Before each measurement, a clean sample surface was prepared. Adsorbed molecules and other adatoms were removed by sputtering-cleaning the surface with 1 kV Ar^+ Ions ($p_{\text{Ar}} = 8 \times 10^{-6}$ mbar, $I = 1.8 \mu\text{A}$, $t = 10$ min). After sputtering the samples were annealed to get a regular surface termination.

For $\text{Fe}_2\text{O}_3(012)$ two surface terminations exist that can be easily prepared. The (1×1) termination, which is generally agreed to be a bulk terminated surface [65], was prepared by annealing the sample in oxygen ($p_{\text{O}_2} = 1 \times 10^{-6}$ mbar, $t = 30$ min, $T = 550$ °C). Figure 20 shows a model of the $\text{Fe}_2\text{O}_3(012)$ - (1×1) surface.

If the sample is annealed in UHV ($p < 1 \times 10^{-9}$ mbar, $T = 570$ °C, $t = 30$ min), the surface forms a (2×1) termination instead. Figure 21 shows a comparison of two LEED images of the respective surfaces. The exact nature of this (2×1) surface reconstruction is not completely clear yet. Efforts to unravel the reconstruction have been made in the past [66], though recent developments (LEED-IV measurements and DFT calculations) have shown that model to be incorrect.

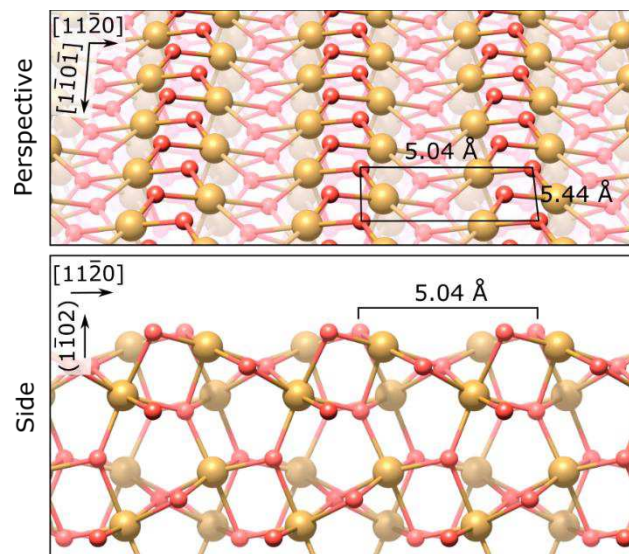


Figure 20: Model of the $\text{Fe}_2\text{O}_3(012)$ (1×1) surface. Both a top view and a side view are presented. The unit cell is marked in the image and measures $0.504 \times 0.544 \text{ nm}^2$.

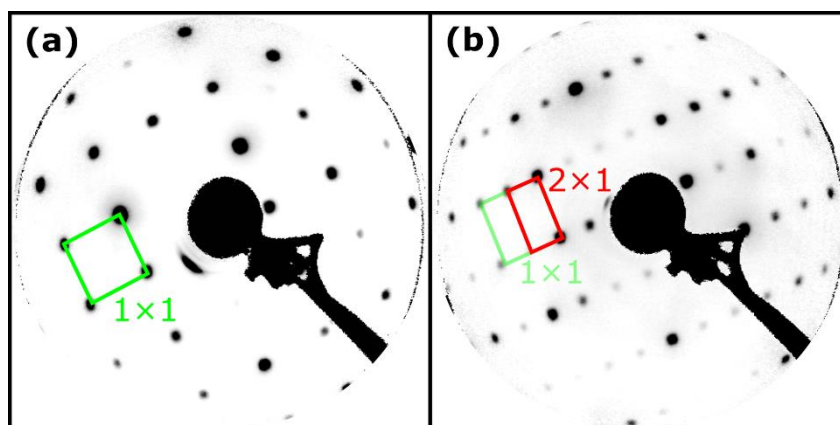


Figure 21: LEED patterns obtained from the $\text{Fe}_2\text{O}_3(012)$ (1 \times 1) (a) and (2 \times 1) (b) surface reconstructions ($U = 1$ kV, beam energy: 100 eV). The respective unit cells in reciprocal space are marked.

Even if the exact surface reconstruction is unknown, certain aspects are well known through experiment. XPS, UPS and EELS measurements have shown the presence of Fe^{2+} on the (2 \times 1) surface [67]. This feature is missing entirely from the (1 \times 1) termination and shows the (2 \times 1) to be in a more reduced state.

It should be noted that it is possible to switch between the two surface terminations by annealing the sample in UHV ((1 \times 1) \rightarrow (2 \times 1), $T \approx 570$ °C, $t = 15$ min) or in oxygen ((2 \times 1) \rightarrow (1 \times 1), $T = 550$ °C, $p_{\text{O}_2} = 1 \times 10^{-6}$ mbar, $t = 30$ min) respectively.

5.3 Results

5.3.1 The clean surface

Figure 22 shows STM images of four clean sample surfaces ($26 \times 26 \text{ nm}^2$). While the atomic structure is the same on all three images, some large defects can be seen on Figure 22c and Figure 22d. These features (marked in yellow) stem from the Ti-doping, the titanium incorporates in the second layer forming these characteristic “trenches”. The ultra-low-doped film (0.03 at% Ti) also shows some of these characteristic defects, albeit they seem to be rarer and mostly appear as singular point defects (Figure 22b). While the undoped single crystal also shows several dark spots on the surface when scanned with a positive sample bias, (Figure 22a) these do not stem from titanium doping but are rather occurring naturally. Their origin not yet known. Crystal defects, adsorbates or other kind of impurities could lead to the different contrast as seen in STM.

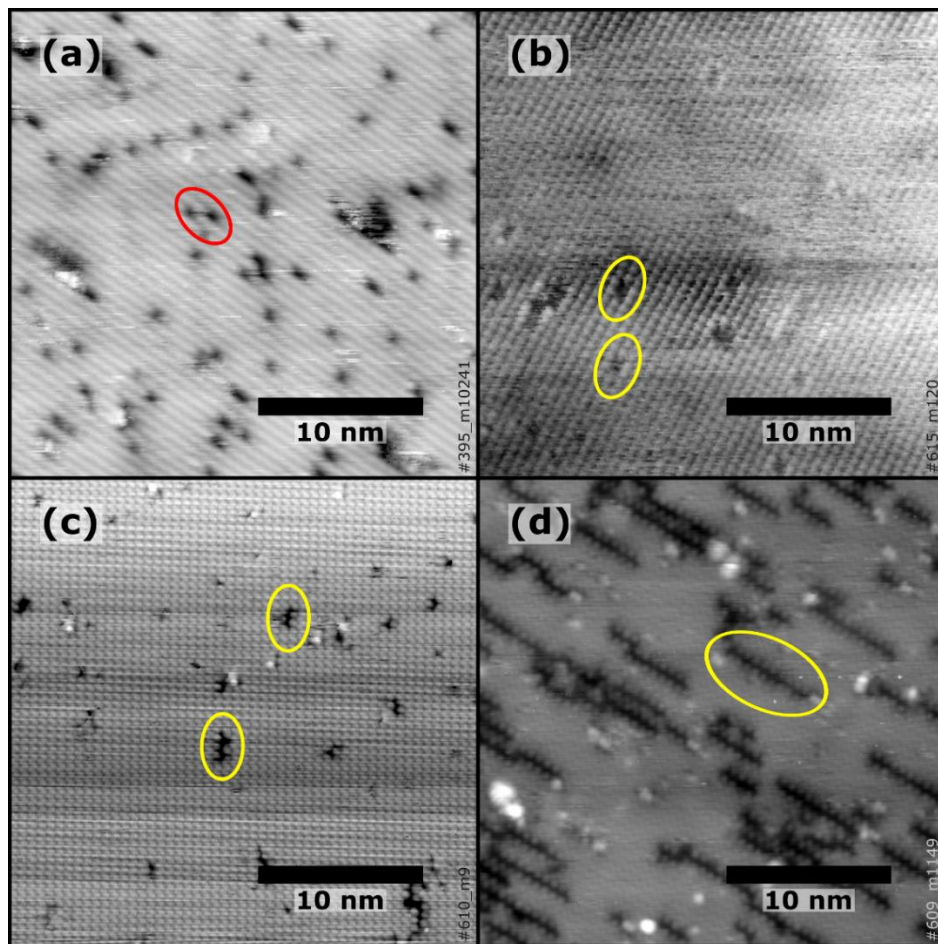


Figure 22: STM images of the clean $\text{Fe}_2\text{O}_3(012)$ (1×1) surfaces ($26 \times 26 \text{ nm}^2$; a: $U = 2.5 \text{ V}$, $I = 0.22 \text{ nA}$; b: $U = 1.8 \text{ V}$, $I = 0.3 \text{ nA}$; c: $U = 2.8 \text{ V}$, $I = 0.3 \text{ nA}$; d: $U = 1.8 \text{ V}$, $I = 0.1 \text{ nA}$). While (a) shows a big terrace of the undoped single crystal surface, (b-d) show Ti-doped thin films with Ti doping levels of 0.03 at% (b), 0.8 at% (c) and 3.1 at% (d) respectively. Some titanium-induced surface defects are marked in yellow. The defects on the undoped crystal (marked in red) do not stem from titanium doping but are naturally occurring. They can be observed while scanning with a positive bias, but their origin is yet unknown.

When scanning a surface with STM, a positive or a negative bias can be applied to image empty or filled states of the sample respectively. This allows imaging of the Fe-lattice with a positive bias and of the surface oxygen with a negative bias, though the images resemble each other, since both atom species are arranged in a zig-zag pattern [66].

Interestingly, scanning the hematite (1×1) surface with a negative bias was observed to result in an accumulation of bright protrusions at the scanned region. To test this hypothesis, a large STM image (100 × 100 nm²) was recorded with a positive bias. Then a small section of the previously scanned region (≈30 × 30 nm²) was scanned multiple times with a negative bias. Finally, the image size was increased, and the initial large region was recorded again with a positive bias. Figure 23 shows a comparison of the images of the large regions before and after scanning the small region with a negative bias. Figure 23b clearly shows an increased number of protrusions in the region that was scanned with a negative bias (yellow outline). If the experiment is repeated but the small area is scanned with a positive bias instead, the effect is negligible. Figure 23c shows an STM image where the central part highlighted in red was scanned multiple times using a positive bias.

The reason for this increased formation of adatoms on the surface is still unknown.

It is interesting that the (2×1) surface termination of Fe₂O₃(012) does not show this behaviour, though there is a natural degeneration of the (2×1) surface as it is very hydrophilic which leads to an accumulation of water on the surface even in UHV conditions.

As this work is focussed on the (1×1) termination, the sample surface was preferentially scanned using a positive bias to avoid the scanning-induced formation of protrusions.

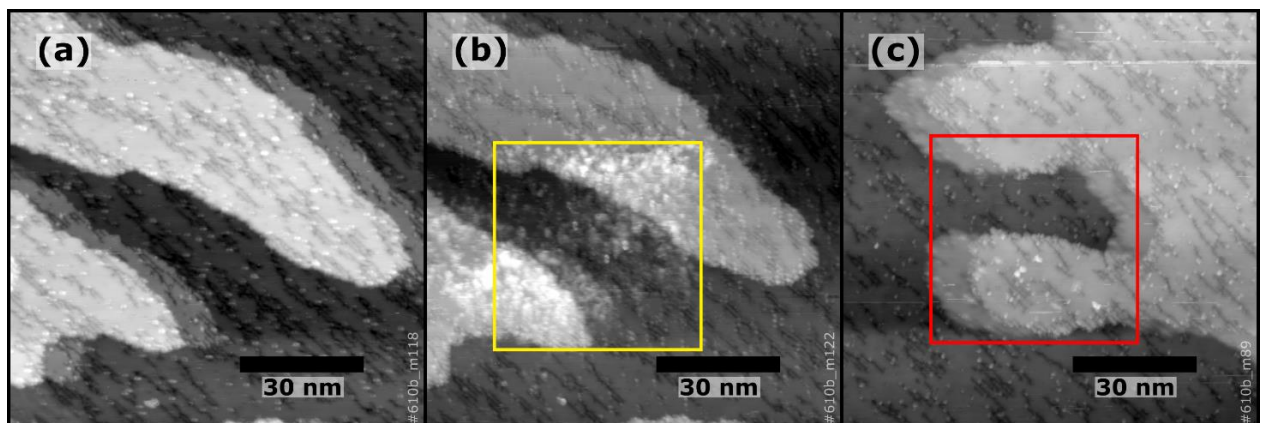


Figure 23: STM images of a Ti-doped Fe₂O₃(012) (1×1) surface (100 × 100 nm²; a, b: U = 2.7 V, I = 0.26 nA; c: U = 2.5 V, I = 0.25 nA). (a) shows an image of the clean sample surface, (b) shows the same area after a smaller region in the center (30 × 30 nm², outlined in yellow) was scanned three times with U = −2.7 V and I = 0.26 nA. After the scans with a negative bias, multiple protrusions are visible on the surface, clearly outlining the scanned region. When the same experiment is repeated with a positive bias, no such effect is noticeable. (c) shows an image where the central region outlined in red was scanned 11 times.

5.3.2 Surface defects

Surface defects present possible anchor sites for adatoms. Before deposition, such defects could be generated purposefully to create adsorption sites for deposited metal atoms. To achieve this, a reliable and reproducible way to generate such defects is required. Oxygen vacancies are a plausible defect on any given metal oxide. To achieve a higher density of oxygen vacancies on the surface, the surface can be hydroxylated via exposure to atomic hydrogen. Subsequent annealing at temperatures of ≈ 200 °C leads to a desorption of water, extracting surface oxygen atoms resulting in oxygen vacancies.

Preliminary studies have been conducted on grown Fe_2O_3 thin films with a very high Ti-doping percentage (3.1 at%). Such high-doped films have not proven ideal for the studies as their surface is dominated by Ti-induced surface defects, making a reliable identification of additional surface defects challenging. Figure 24 shows images of the clean sample surface.

To expose the surface to atomic hydrogen, the preparation chamber is flooded with hydrogen gas. A hydrogen cracker situated near the sample breaks the H_2 bonds, resulting in single hydrogen atoms adsorbing on the surface. The hydroxylated surface was scanned after hydrogen exposure. Figure 25 shows images of the surface after hydrogen deposition and post heating the hydroxylated surface to 200 °C. To facilitate the generation of point defects, a lower dosage was used for the annealed sample shown in Figure 25b than can be seen in the Figure 25a.

Imaging the hydroxylated surfaces proved to be difficult. At room temperature the deposited hydrogen atoms seem to be quite mobile, leading to large regions without any discernible resolution. After the heating process, the surface does show some point defects, though it is hard to quantify and compare the number of defects to a clean surface as both surfaces are covered in titanium-induced defects. Hydrogen could simply recombine to H_2 and desorb without effecting the surface oxygen. To unambiguously show if hydroxylation and annealing has an effect at all on the hematite surface, experiments on a different sample – preferably with a lower Ti-doping percentage – are required.

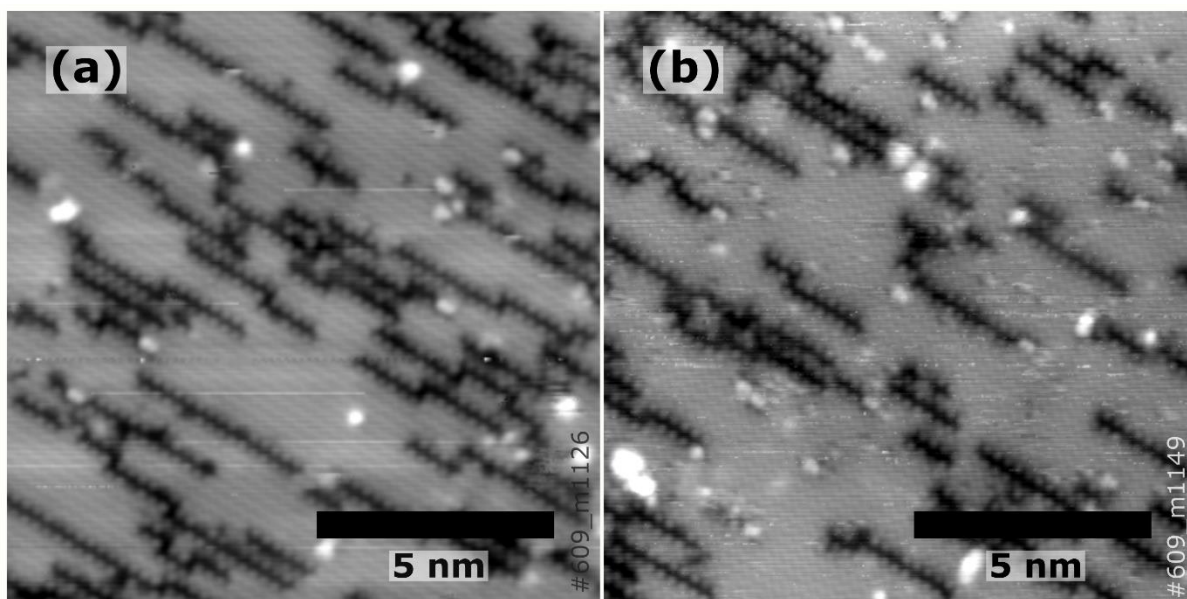


Figure 24: STM images of the clean, 3.1 at% Ti-doped $\text{Fe}_2\text{O}_3(012)$ (1×1) surface ($26 \times 26 \text{ nm}^2$; a: $U = 2.5 \text{ V}$, $I = 0.2 \text{ nA}$; b: $U = 1.8 \text{ V}$, $I = 0.1 \text{ nA}$). The surface is dominated by the trench like titanium defects along the rows. Additionally, several bright protrusions can be seen on the surface, suggesting some amount of adsorbates present.

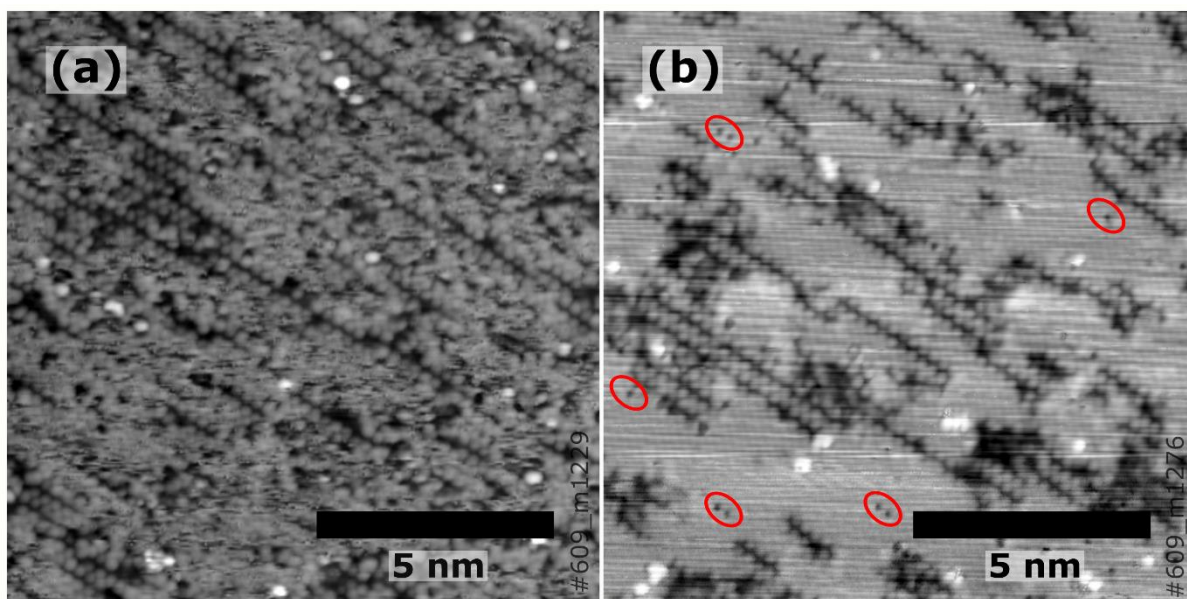


Figure 25: STM images of the 3.1 at% Ti-doped $\text{Fe}_2\text{O}_3(012)$ (1×1) surface ($26 \times 26 \text{ nm}^2$; a: $U = 2.2 \text{ V}$, $I = 0.2 \text{ nA}$; b: $U = 2.3 \text{ V}$, $I = 0.3 \text{ nA}$). (a) shows the hydroxylated surface after exposure to atomic hydrogen ($p_{\text{H}_2} = 2 \times 10^{-6} \text{ mbar}$, 30 min). Large regions show no discernible resolution, suggesting mobile species on the surface.

(b) shows a previously hydroxylated surface ($p_{\text{H}_2} = 1 \times 10^{-6} \text{ mbar}$, 5 min) that was heated to $200 \text{ }^\circ\text{C}$ to remove the hydrogen, hoping to generate additional oxygen vacancies in the process. Possible point defects are marked in red, though a reliable identification of additional surface defects proved challenging because the surface is dominated by Ti-induced defects.

An electron gun can be used as an alternate way to generate surface defects. An electron beam is accelerated towards the sample surface, which leads to local beam damage of the affected

region. The electron energy can be tuned which could give a control of the number of generated defects [68]. Also, the size of the beam spot can be controlled, which enables reference experiments on the surface of the same sample.

As with the H deposition, preliminary data using an e-gun was collected. After electron bombardment, the surface was covered in protrusions, making an identification of possible added oxygen vacancies almost impossible. Figure 26 shows an STM image of the sample surface after exposure to the electron beam for 5 minutes. The possible oxygen vacancies are marked. It is possible that the experiment could be performed in a cleaner way by additional outgassing of the electron gun filament. The image was recorded with a double tip, meaning the number of surface protrusions is likely lower than it appears. Protrusions could also stem from adsorbates that react with generated oxygen vacancies.

While these preliminary results are promising, additional experiments – preferably on an ultra-low Ti-doped thin film – for both methods of defect generation are required to ultimately achieve a controlled predictable way of surface defect generation.

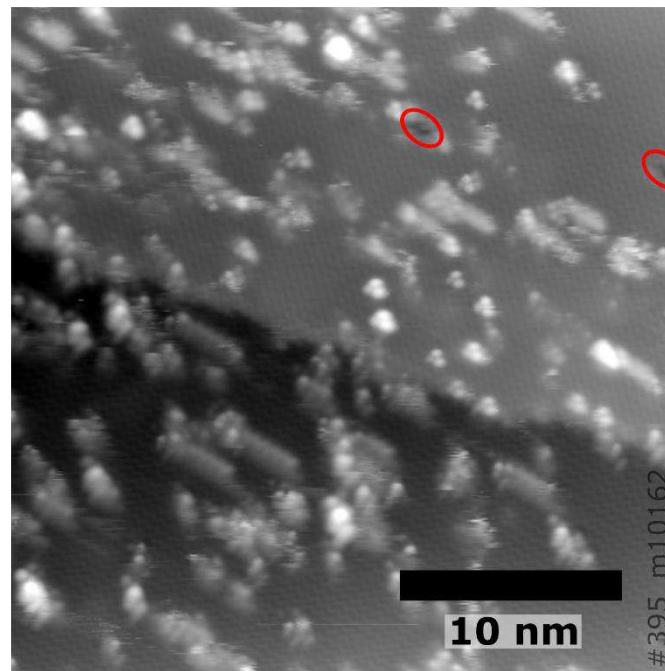


Figure 26: STM images of the undoped $\text{Fe}_2\text{O}_3(012)$ (1×1) surface after electron bombardment ($30 \times 30 \text{ nm}^2$; $U = -2.4 \text{ V}$, $I = 0.24 \text{ nA}$; e-gun: $I_{\text{em}} = 25 \mu\text{A}$; $U_{\text{a}} = 3 \text{ kV}$, 5 min). While some defects are visible (marked in red), many protrusions cover the surface post electron bombardment.

5.3.3 Rhodium deposition

For achieving realistic SAC systems, the stability of adatoms on the support system must be studied. Here rhodium deposited at different coverages onto the hematite (012) (1×1) termination is discussed.

To avoid the influence of the titanium-induced defects, most of the data was recorded on the undoped single crystal. A reference experiment on the ultra-low-doped thin film showed that data can be reproduced on doped samples as well.

A metal evaporator was used for the deposition process. There, a Rh metal rod is heated with an electron beam and is evaporated at the tip of said rod. To avoid an acceleration of charged particles towards the sample through the electric field of the electron gun, a compensation field is applied. Thus, only uncharged particles reach the sample surface. To discern the deposited amount, a quartz crystal microbalance was used. The amount of deposited metal was measured in percentages of a monolayer (ML) where 1 monolayer means 1 atom per $\text{Fe}_2\text{O}_3(012)$ (1×1) unit cell ($0.504 \times 0.544 \text{ nm}^2$).

0.05 ML Rh were deposited on the clean hematite (1×1) surface. XPS spectra of the Rh 3d region were recorded before and after the deposition. The sample was then annealed at 200 °C, 300 °C, 400 °C and 500 °C respectively. The usual heating duration was 15 minutes, only for the highest temperature of 500 °C a shorter duration of 10 min was chosen. After each heating process, XPS spectra were obtained. Figure 27 shows the XPS data of the temperature series. The same experiment was repeated with a coverage of 0.2 ML Rh and with a coverage of 0.05 ML Rh on a titanium-doped sample (0.03 at% Ti).

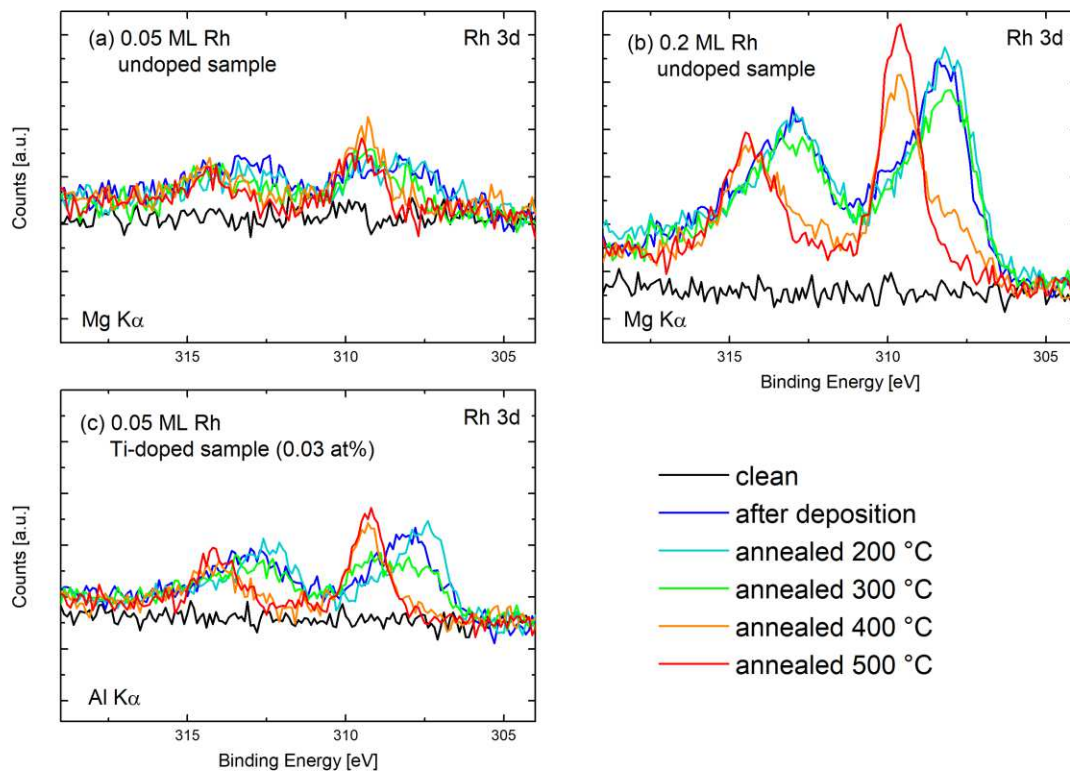


Figure 27: XPS spectra of the Rh 3d region after deposition of Rh on the $\text{Fe}_2\text{O}_3(012)$ (1 \times 1) surface (a, b: Mg anode; c: Al anode; 70° emission). (a) and (b) show different coverages of Rh on an undoped single crystal sample while (c) shows a reference experiment conducted on an ultra-low titanium-doped hematite thin film (0.03 at% Ti). After annealing in UHV conditions ($< 1\times 10^{-9}$ mbar) at high temperatures, the Rh peak shifts to lower binding energies.

A rough peak fit – using a Gaussian-Lorentzian peak shape and a Shirley background – was performed to reveal more information such as peak position and full width at half maximum (FWHM). Looking at the temperature series of 0.05 ML Rh on the undoped natural crystal, the Rh 3d 5/2 peak appears at 308.5 eV after deposition. It shows a relatively high broadness with a FWHM of ≈ 3 . After annealing at 200 °C, the FWHM measures ≈ 3.4 and a slight shift to lower binding energies (308.4 eV) is observed. After annealing the sample at 300 °C, the Rh 3d 5/2 peak shows a lower FWHM (2.5) and is shifted to 309.1 eV. Annealing at 400 °C shifts the peak to 309.5 eV with a FWHM of 1.64. After annealing at 500 °C the peak further shifts to 309.6 eV with a FWHM of 1.4, resulting in a peak shift of ≈ 1.1 eV compared to the peak after the initial deposition. It should be noted that the intensity of the measured Rh peaks was low, thus only single peaks were used in the peak fit to gain information about the absolute peak shift and broadening.

The signal for 0.2 ML Rh deposited on the same undoped crystal was higher, resulting in more accurate data. A higher count rate was also achieved on the ultra-low Ti-doped sample, resulting in a better signal to noise ratio for the temperature series with 0.05 ML Rh.

Figure 28 shows a peak fit for selected stages of the temperature series on these two samples. As before, Gaussian-Lorentzian peak shapes (GL(30)) together with a Shirley background were used for the fitting process. Both the Rh 3d 5/2 and Rh 3d 3/2 peak were fitted for each spectrum recorded in the temperature series with the usual area constraint of a factor 0.75 applied. The peak position for the higher binding energy peak was determined from the spectra recorded after annealing at 500 °C. For the other spectra the peak position was fixed to this value, only allowing for small deviations of ± 0.1 eV. No positional constraints were set for the lower energy peak. In each spectrum, both 5/2 and 3/2 peaks were set to have the same FWHM respectively. The 3/2 peaks of the Rh 3d region generally show a slightly higher FWHM due to the Coster-Kronig effect. The distance between the 5/2 and 3/2 peaks was constrained to be 4.7 eV according to literature [69].

While these parameters yield peak fits with reasonably low residual standard deviation (typically < 0.9), caution should be exercised as they do present a severe simplification of the real system. The peak positions of a measured Rh species can shift if Rh atoms form clusters, as measured binding energy in XPS has been shown to decrease with increasing cluster size [70].

For both samples the spectrum after the initial Rh deposition and after annealing at 500 °C is shown. The displayed data for the stage in between shows a different temperature, 400 °C for the undoped and 300 °C for the ultra-low doped sample. This was chosen to show spectra where a transition from the metallic to the oxide peak is best visible. As all temperatures were measured with a thermocouple situated close to the sample on the sample holder, the actual sample temperatures likely differ. Due to different sample mounting geometries, the actual sample temperature of the ultra-low-doped sample is probably higher than the readout suggests. This can be most likely attributed to the hole in the sample plate, which allows the electron beam to directly heat the hematite crystal. Assuming a higher temperature in comparison to the undoped sample could explain the earlier onset of the peak shift to higher binding energies.

Looking at 0.2 ML Rh on the undoped crystal, the Rh 3d 5/2 peak appears at 308.2 eV after deposition and shows a profound shoulder towards higher binding energies. The peak fit suggests a contribution from a second peak at 309.7 eV, associated with oxidized Rh. After annealing at 400 °C the peak is shifted to higher binding energies with a shoulder towards lower binding energies. The peak fit reveals a higher contribution of the oxide peak situated at

309.6 eV and a lower contribution from the metallic Rh peak, now situated at 307.8 eV. Annealing at 500 °C leads to a symmetric peak shape with a peak position at 309.6 eV resulting in a peak shift of ≈ 1.4 eV compared to the peak after deposition.

For 0.05 ML Rh deposited onto the ultra-low Ti-doped sample, the results are similar:

After deposition an asymmetric peak with a shoulder towards higher binding energies is measured at 308 eV. The peak fit suggests a small oxide peak at 309.4 eV as the origin of said shoulder. Annealing at 300 °C leads to a very broad double peak that can be explained with two almost identically sized peaks, positioned at 307.6 eV and 309.3 eV respectively. After annealing at 500 °C the peak is symmetric in shape and situated at 309.3 eV, resulting in a peak shift of ≈ 1.3 eV compared to the peak after deposition.

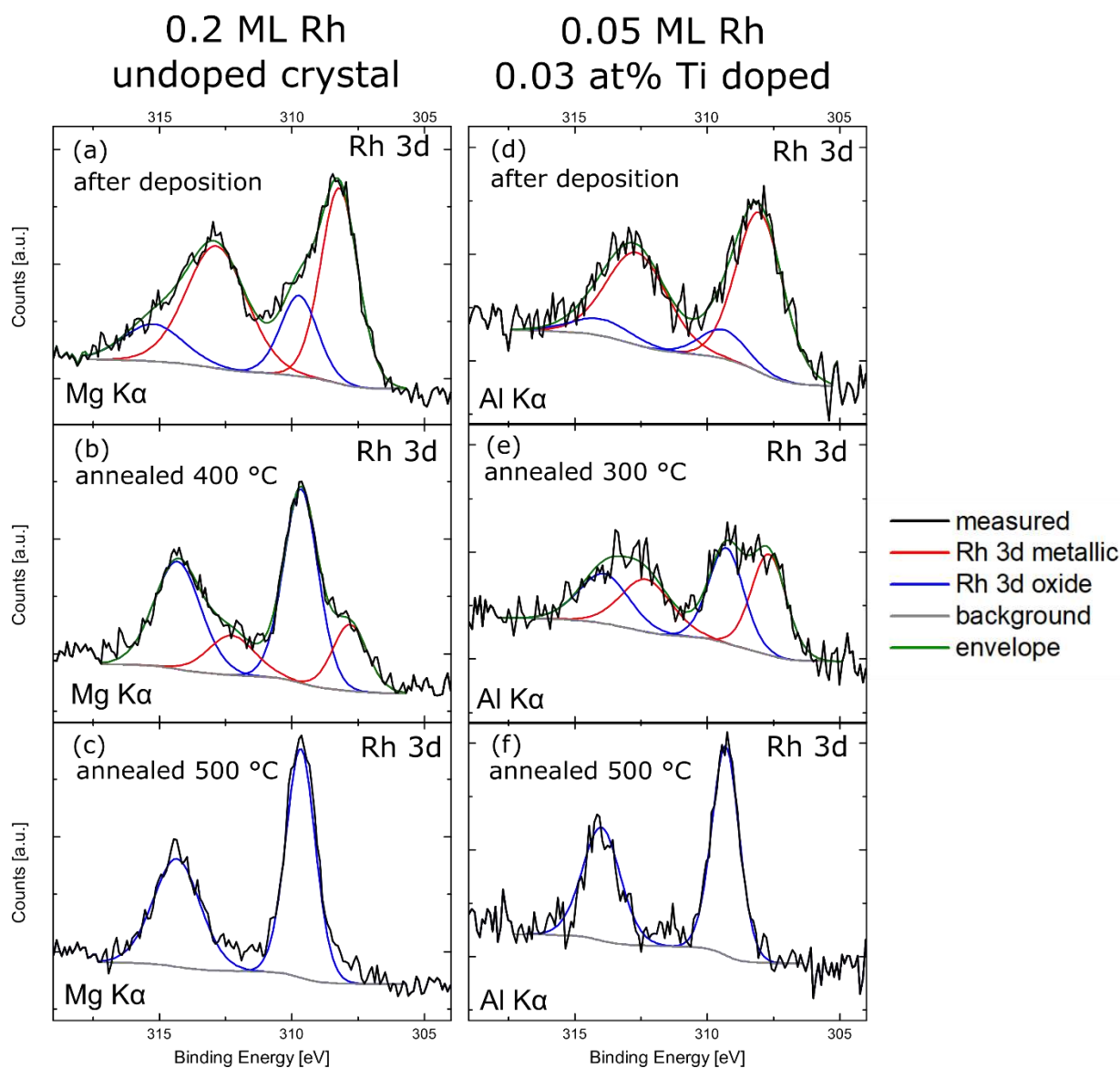


Figure 28: XPS spectra of the Rh 3d region after deposition of Rh on the $\text{Fe}_2\text{O}_3(012)$ (1 \times 1) surface with peak fits (a, b, c: Mg anode; d, e, f: Al anode; 70° emission). (a), (b) and (c) show three different states of the temperature series of 0.2 ML Rh on an undoped hematite crystal (Figure 27a). (d), (e) and (f) show three different states of the temperature series of 0.05 ML Rh on a 0.03 at% Ti-doped sample (Figure 27c). Peak positions after deposition are 308.2 eV and 308.0 eV, respectively. The peak fit reveals a contribution of two peaks for the spectra right after deposition and after annealing at 400 °C or 300 °C. The peak with a lower binding energy is associated with metallic Rh, while the peak with a higher binding energy is associated with oxidized Rh. After annealing at 500 °C the peak shape is symmetric, only showing contribution from the higher energy peak (309.6 eV for (c) and 309.3 eV for (f)) resulting in a peak shift of 1.4 eV (c) or 1.3 eV (f) when compared to the peaks after deposition.

STM images of the deposition and annealing process were recorded and are presented in the following section. All images presented in Figure 29-Figure 31 were recorded with a positive sample bias to avoid the formation of additional protrusions through the scanning process.

While the sample size is small and – depending on image quality – it is not always clear what counts as a single protrusion, the protrusions on the presented images were counted and their height determined to gain as much statistical information as possible about the deposition process. Table 3 shows a summary of the statistical information gathered for the recorded images.

sample	undoped	undoped	undoped	undoped	undoped	undoped	doped	doped	doped
coverage [ML]	0.2	0.2	0.2	0.05	0.05	0.05	0.05	0.05	0.05
stage	after deposition	annealed 300 °C	annealed 400 °C	after deposition	annealed 300 °C	annealed 400 °C	after deposition	annealed 300 °C	annealed 400 °C
area density [#nm ⁻²]	0.118	0.083	0.029	0.066	0.033	0.016	0.052	0.027	0.010
height (average) [pm]	131.40	200.95	237.86	154.15	186.36	171.82	38.00	72.78	47.14
standard deviation [pm]	42.43	56.74	98.93	39.75	53.32	49.56	13.46	29.27	9.51
height (median) [pm]	130	190	215	150	175	160	30	70	40
height (mode) [pm]	80	190	180	140	170	160	30	50	40

Table 3: Statistical information about the protrusions measured in Figure 29-Figure 31.

After the deposition of 0.2 ML Rh on the undoped hematite single crystal, multiple bright protrusions can be observed on the surface. These protrusions have an average height of ≈ 131 pm and an area density of 0.118 protrusions per nm². This density is significantly smaller than the theoretical density of 0.2 ML coverage which calculates to 0.729 protrusions per nm². After annealing at 300 °C, the average protrusions height increases to ≈ 201 pm while the area density decreases to 0.08 protrusions per nm². Annealing at 400 °C leads to a similar average protrusion size of ≈ 238 pm though with a higher standard deviation as more protrusions showed a height of above 300 pm. Fewer bright protrusions are visible with a density of 0.03 protrusions per nm². After annealing the sample for 10 minutes in UHV, the previously observed large protrusions seem to have vanished, leaving behind an almost clean looking hematite (1×1) surface.

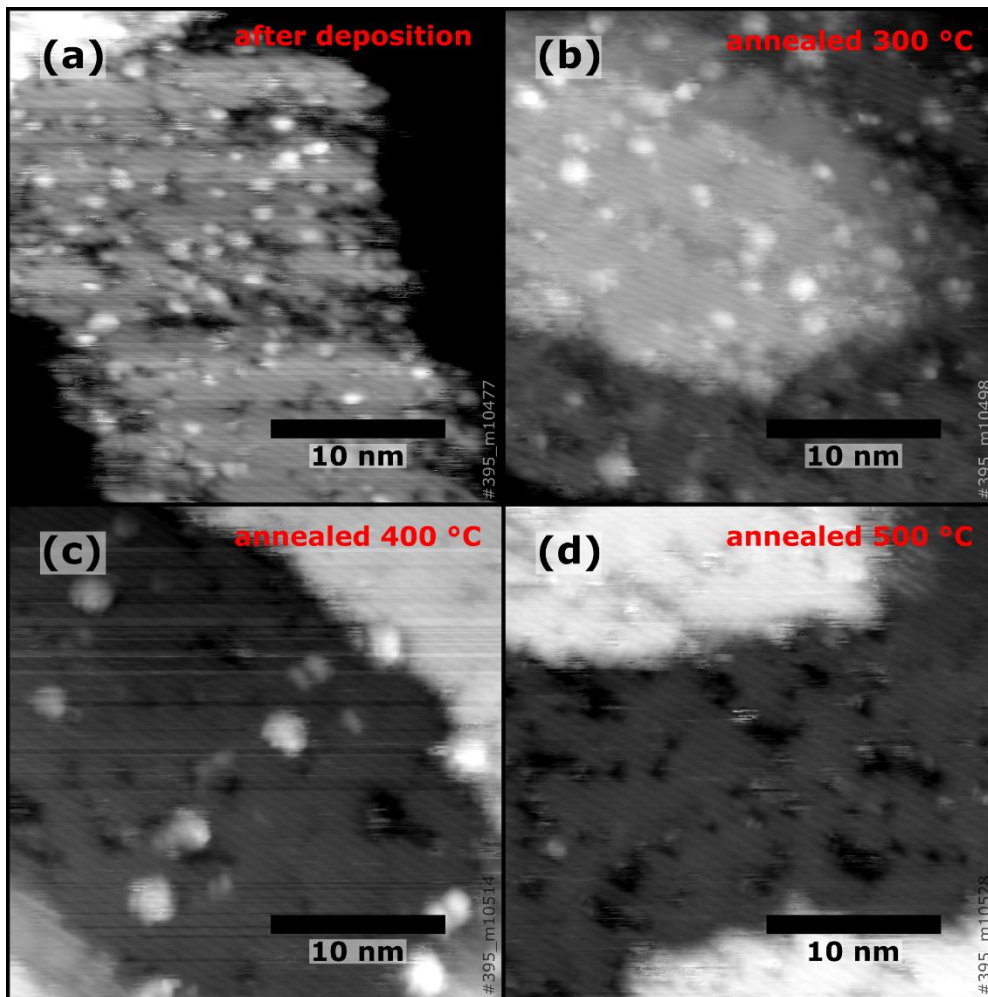


Figure 29: STM images of 0.2 ML Rh deposited on an undoped $\text{Fe}_2\text{O}_3(012)$ (1×1) surface ($26 \times 26 \text{ nm}^2$; a: $U = 2.2 \text{ V}$, $I = 0.1 \text{ nA}$; b: $U = 2.0 \text{ V}$, $I = 0.1 \text{ nA}$; c: $U = 1.8 \text{ V}$, $I = 0.1 \text{ nA}$; d: $U = 1.8 \text{ V}$, $I = 0.1 \text{ nA}$). Bright protrusions are visible after deposition (a: average height: 131.4 pm, area density: 0.118 $\#/\text{nm}^2$). Annealing the sample in UHV conditions at 300 °C for 15 minutes results in slightly fewer, higher protrusions (b: average height: 201.0 pm, area density: 0.083 $\#/\text{nm}^2$). After annealing at 400 °C for 15 minutes even less protrusions are visible on the surface (c: average height: 237.9 pm, area density: 0.029 $\#/\text{nm}^2$). Annealing at 500 °C for 10 minutes leads to a seemingly clean surface with hardly any protrusions left.

The experiment was repeated for a coverage of 0.05 ML Rh on the same undoped hematite surface. After deposition, bright protrusions with an average height of $\approx 154 \text{ pm}$ and an area density of 0.07 protrusions per nm^2 can be observed. Again, this density is lower than the theoretical coverage of 0.05 ML would suggest (0.182 protrusions per nm^2). As before, the number of protrusions diminishes with higher annealing temperatures. After annealing at 300 °C, the protrusions show an average height of $\approx 186 \text{ pm}$ with a density of 0.03 protrusions per nm^2 . After annealing at 400 °C the average height of the observed protrusions was $\approx 178 \text{ pm}$ with an area density of 0.02 protrusions per nm^2 . After annealing at 500 °C the surface looks clean, without any protrusions visible. Compared to the higher coverage of 0.2 ML Rh, the protrusion size did not increase as much during the annealing process while the area density

decreased similarly. Other than the experiment with 0.2 ML Rh, the temperature series was recorded over multiple days.

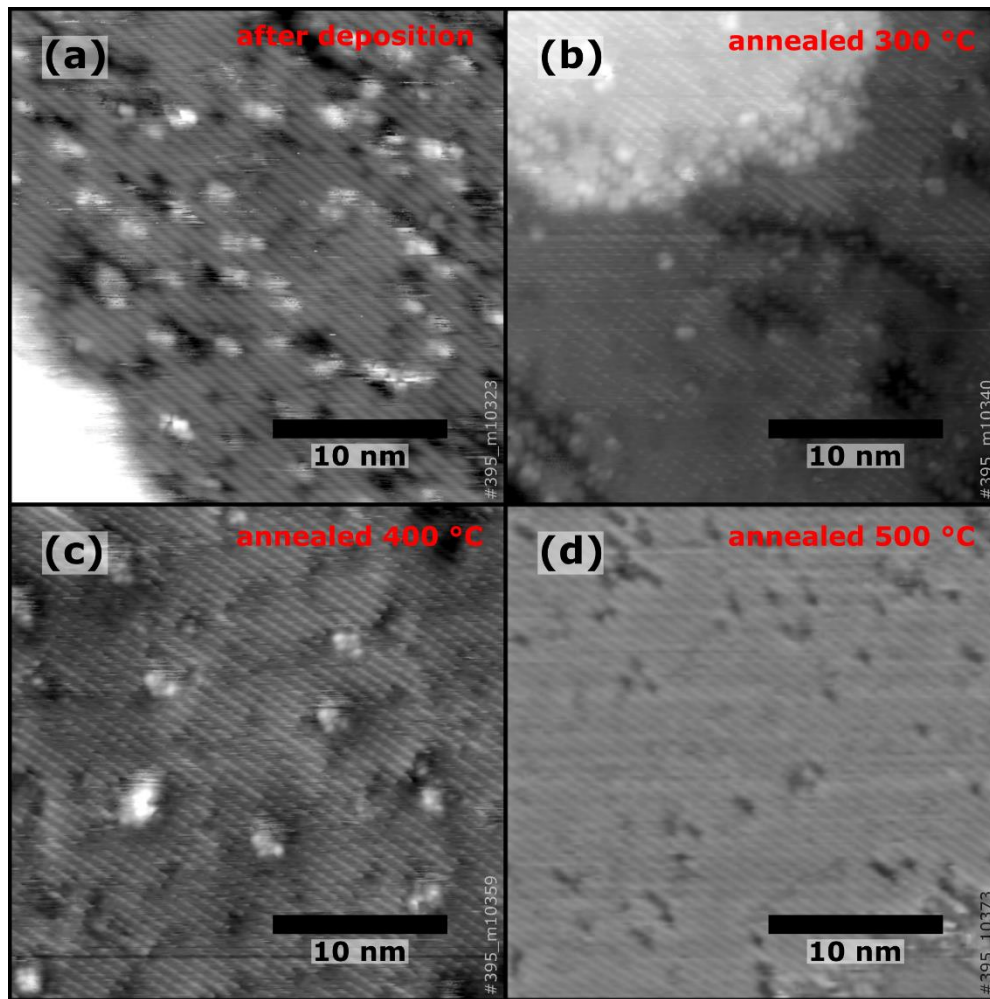


Figure 30: STM images of 0.05 ML Rh deposited on an undoped $\text{Fe}_2\text{O}_3(012)$ (1×1) surface ($26 \times 26 \text{ nm}^2$; a: $U = 2.6 \text{ V}$, $I = 0.2 \text{ nA}$; b: $U = 2.0 \text{ V}$, $I = 0.2 \text{ nA}$; c: $U = 2.0 \text{ V}$, $I = 0.1 \text{ nA}$; d: $U = 2.0 \text{ V}$, $I = 0.2 \text{ nA}$). Bright protrusions are visible after deposition (a: average height: 154.2 pm, area density: 0.066 $\#/\text{nm}^2$). Annealing the sample in UHV conditions at 300 °C for 15 minutes leads to a reduction in protrusion number (b: average height: 186.4 pm, area density: 0.033 $\#/\text{nm}^2$). After annealing at 400 °C for 15 minutes few protrusions are visible on the surface (c: average height: 171.8 pm, area density: 0.016 $\#/\text{nm}^2$). Annealing at 500 °C for 10 minutes leads to a seemingly clean surface with hardly any protrusions left.

The experiment with 0.05 ML Rh coverage was repeated on the ultra-low Ti-doped thin film sample (0.03 at% Ti). Small protrusions can be observed after the deposition process with an average height of $\approx 38 \text{ pm}$ and an area density of 0.052 protrusions per nm^2 . Annealing at 300 °C halves this area density (0.027 protrusions per nm^2) while increasing the average protrusion height to $\approx 73 \text{ pm}$. The protrusion height at this stage shows a high variance and thus has a high standard deviation. After annealing at 400 °C the average protrusions height measures $\approx 47 \text{ pm}$ with an area density of 0.01 protrusions per nm^2 . Annealing at 500 °C leads to a seemingly clean surface with very little protrusions. The presented data was recorded over

the course of several days. While the sample was stored overnight in an UHV environment with a pressure of $< 7 \times 10^{-11}$ mbar, an influence on the experiment cannot be ruled out.

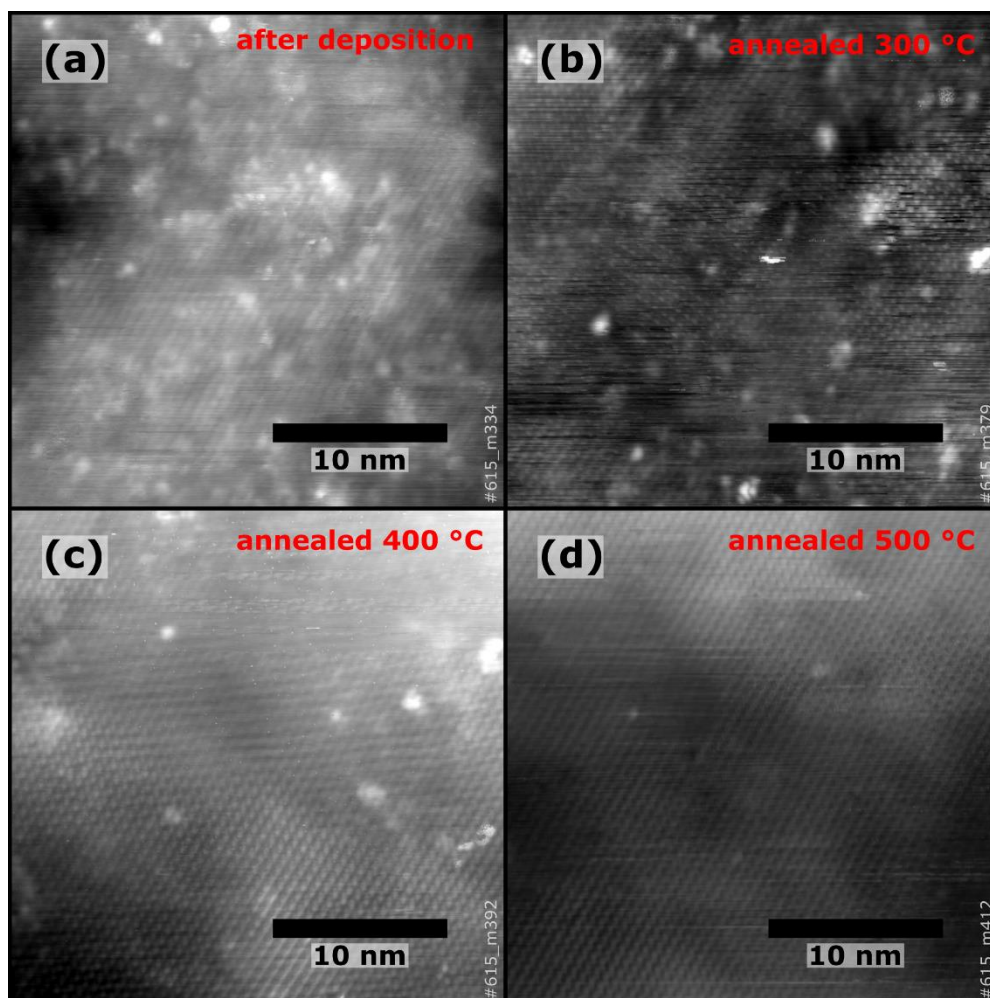


Figure 31: STM images of 0.05 ML Rh deposited on a 0.03 at% titanium-doped $\text{Fe}_2\text{O}_3(101)$ (1×1) surface ($26 \times 26 \text{ nm}^2$; a: $U = 2.6 \text{ V}$, $I = 0.29 \text{ nA}$; b: $U = 2.8 \text{ V}$, $I = 0.26 \text{ nA}$; c: $U = 2.8 \text{ V}$, $I = 0.28 \text{ nA}$; d: $U = 2.8 \text{ V}$, $I = 0.28 \text{ nA}$). Bright protrusions are visible after deposition (a: average height: 38.0 pm, area density: 0.052 \#/nm^2). Annealing the sample in UHV conditions at 300 °C for 10 minutes leads to a reduction in protrusion number (b: average height: 72.8 pm, area density: 0.027 \#/nm^2). After annealing at 400 °C for 10 minutes even fewer protrusions are visible on the surface (c: average height: 47.1 pm, area density: 0.010 \#/nm^2). Annealing at 500 °C for 5 minutes leads to a seemingly clean surface with few protrusions left.

Comparing the data of the undoped and the ultra-low Ti-doped sample, the average protrusion height seems to be significantly smaller on the latter sample. Caution is advised when directly comparing these measurements, as image quality, measurement parameters and tip condition can influence the acquired data.

The STM images directly after Rh deposition on the ultra-low Ti-doped sample were of mediocre quality. Figure 32 shows an STM image with very good resolution, recorded on the same sample after annealing at 100 °C for 5 minutes. The surface shows the typical zig-zag rows of the hematite (1×1) reconstruction. Point defects are visible on the surface and are

marked in yellow. They resemble defects found on the clean sample surface and could be Ti-induced defects. The average height of the bright protrusions was measured to be ≈ 134 pm which is significantly higher compared to the average protrusion height in Figure 31 and is rather comparable to average protrusion heights on the undoped sample (Figure 29, Figure 30).

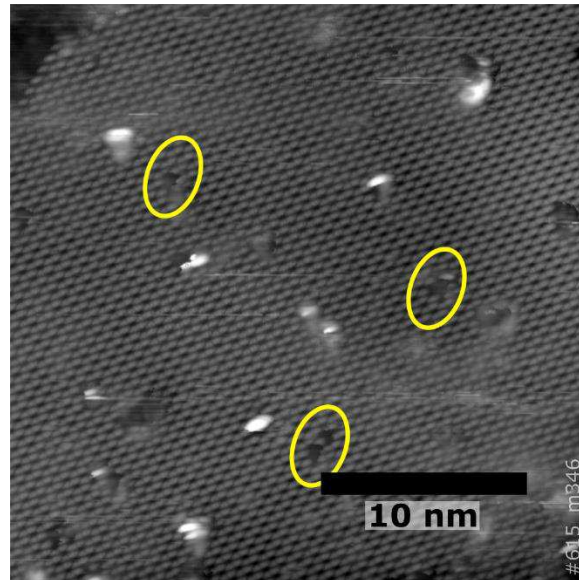


Figure 32: STM image of 0.05 ML Rh deposited on a 0.03 at% titanium-doped $\text{Fe}_2\text{O}_3(012)$ (1×1) surface ($26 \times 26 \text{ nm}^2$; $U = 2.6 \text{ V}$, $I = 0.25 \text{ nA}$). The sample was annealed for 5 minutes at $100 \text{ }^\circ\text{C}$ before recording. The underlying Fe rows are clearly visible. Some characteristic point defects are associated with titanium atoms in subsurface layers and are marked in yellow. The bright protrusions show an average height of 133.8 pm with an area density of 0.019 \#/nm^2 .

When measuring the undoped sample surface after the Rh deposition process with a negative bias, it was difficult to collect data as the scanning process led to an additional formation of protrusions. On the ultra-low Ti-doped sample the acquisition process was more successful. A small region was scanned both in positive and negative sample bias (Figure 33). The negative scans revealed additional structures on the surface that were poorly visible with a positive sample bias. After each negative image, a positive image of the same region was taken to check if any protrusions formed during the negative scan. As no apparent difference was observed, a negative sample bias seems to be feasible for single scans.

Figure 34 shows a larger image ($30 \times 30 \text{ nm}^2$) of the same region, recorded with a negative sample bias. On both images recorded with a negative sample bias, several bright surface features were observed. Some of the protrusions were poorly visible when measuring with a positive sample bias. These protrusions (marked in yellow) have an average height of $\approx 39 \text{ pm}$ and seem to be located on top of the zig-zag pattern of the underlying lattice. Some sections of the zig-zag row appear slightly brighter (marked with red arrows). On the larger image, a large protrusion with a height of $\approx 200 \text{ pm}$ is observed (marked in blue)

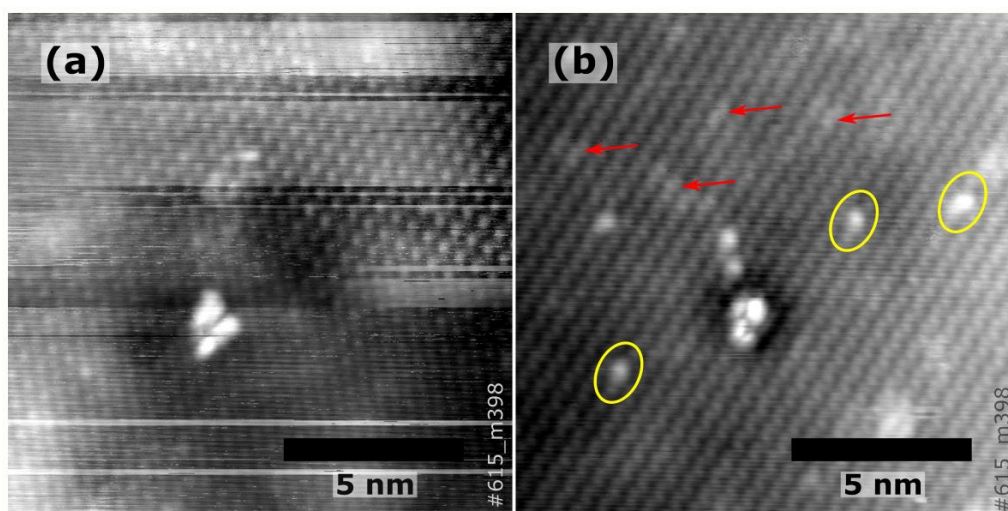


Figure 33: STM images of 0.05 ML Rh deposited on a 0.03 at% titanium-doped $\text{Fe}_2\text{O}_3(012)$ (1×1) surface, after annealing at 400°C in UHV conditions for 10 minutes ($14 \times 14 \text{ nm}^2$; a: $U = 2.6 \text{ V}$, $I = 0.28 \text{ nA}$; b: $U = -2.6 \text{ V}$, $I = 0.28 \text{ nA}$). The same region was inspected with both a positive (a) and a negative (b) sample bias. Additional bright protrusions are visible in image (b). These protrusions appear on top of the zig-zag pattern of the lattice and measure $\approx 39 \text{ pm}$ in height. Some sections of the zig-zag row appear slightly brighter and are marked with red arrows.

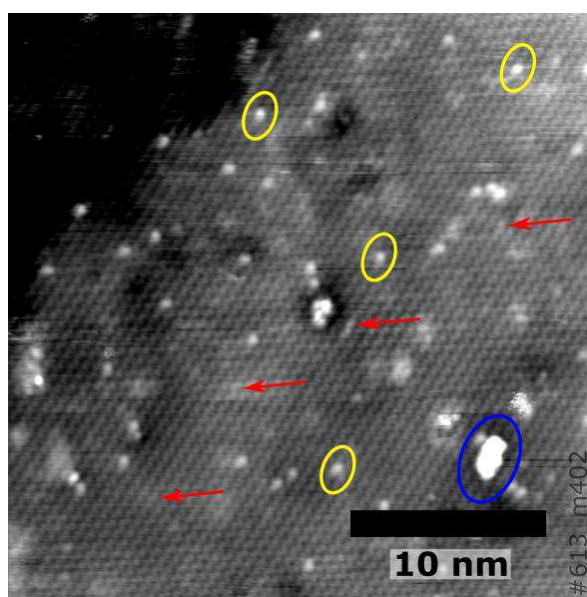


Figure 34: STM image of 0.05 ML Rh deposited on a 0.03 at% titanium-doped $\text{Fe}_2\text{O}_3(012)$ (1×1) surface, after annealing at 400°C in UHV conditions for 10 minutes ($30 \times 30 \text{ nm}^2$; $U = -2.6 \text{ V}$, $I = 0.28 \text{ nA}$). Three types of protrusions can be observed. Protrusions that appear on top of the zig-zag pattern of the lattice are marked in yellow and measure $\approx 39 \text{ pm}$ in height. These protrusions show an area density of 0.051 \#/nm^2 . Some sections of the zig-zag row appear slightly brighter and are marked with red arrows as in Figure 33. An additional large protrusion which measures $\approx 200 \text{ pm}$ in height is marked in blue.

Annealing at even higher temperatures than presented in the temperature series (570°C for the undoped crystal, 550°C for the ultra-low Ti-doped sample) usually leads to a reconstruction of the surface to a (2×1) termination. It is interesting, that after depositing 0.2 ML Rh on the

undoped sample, the phase transition did not occur. LEED still shows a (1×1) pattern after the usual preparation (annealing in UHV for 15 min at 570 °C).

On the ultra-low Ti-doped thin film sample, the experiment was repeated with 0.05 ML Rh. After annealing at the usual preparation settings to achieve a (2×1) surface (annealing in UHV for 15 minutes at 550 °C), LEED images were recorded. The crystal shows a temperature gradient during the annealing process, the upper half of the crystal seems to be always colder than the lower half. This can be observed optically using a camera to monitor glowing (Figure 35). After the annealing process, the lower temperature region, shows a clear (1×1) LEED pattern while the hotter region of the crystal shows a (2×1) pattern. While the exact temperature difference between the two regions is yet unclear, annealing under these conditions without Rh present always resulted in a clear (2×1) pattern on all regions of the crystal.

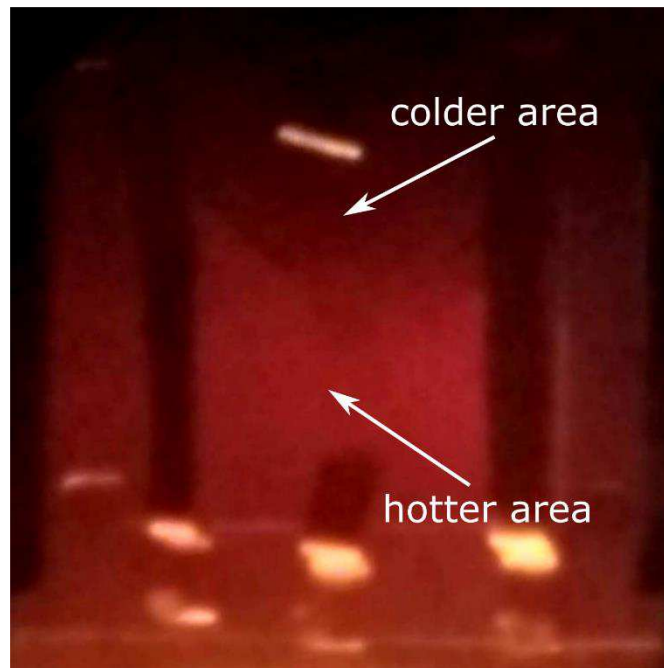


Figure 35: Camera image of the glowing sample surface during an annealing process (520 °C). The upper part of the sample shows a weaker light emission than the lower part, suggesting a lower temperature. The contrast and brightness of the image was adjusted to highlight the difference in brightness.

5.4 Discussion

When interpreting the recorded data of the rhodium deposition process, one must keep in mind that the temperatures readouts are not the same for different samples. The ultra-low Ti-doped thin film sample has a hole in the back of the sample plate, allowing the electron beam to heat the crystal directly. This probably results in a higher sample temperature at the same thermocouple readout compared to the undoped single crystal sample.

The recorded XPS data of the Rh deposition process reflects that. As shown in Figure 27 the Rh peak shifts towards higher binding energies during the annealing process. The onset of this peak shift happens earlier for the ultra-low Ti-doped sample than for the undoped crystal. Besides this difference, the peak fit (Figure 28) shows a similar behaviour on both crystals. The higher energy peak can be associated with oxidized Rh, the lower energy peak with metallic Rh species. After deposition, a mixture of oxidized and metallic species is measured for all three samples. As reported in Table 3, the initial number of measured protrusions was lower than the theoretical Rh coverages would suggest. While there is a possible uncertainty due to the metal deposition process, previous experiments on magnetite surfaces have shown the deposition method to be precise and reliable. For the experiment with 0.2 ML Rh on the undoped crystal, 0.05 ML Rh on the undoped crystal and 0.05 ML Rh on the ultra-low Ti-doped sample, the measured number of protrusions were a factor of 6.2, 2.8 and 3.5 off the theoretical values, respectively. This suggests some amount of sintering of the deposited Rh species. The sample with the highest coverage (0.2 ML Rh) showed the largest discrepancy, possible because higher coverages facilitate the sintering process.

For coverages of 0.05 ML Rh, the average height of protrusions does not seem to be correlated to the annealing temperature. On the sample with a Rh coverage of 0.2 ML Rh, annealing at 300 °C lead to an increase in average protrusion height of $\approx 50\%$ compared to the height after deposition, again suggesting an easier sintering process on this sample.

Annealing at higher temperatures (300 °C and 400 °C) leads to a decrease in protrusion area density on all samples. While this could be explained partially by a sintering process, clusters would usually show a metallic contribution in XPS as the inner atoms dominantly bind with each other rather than with oxygen. However, the recorded XPS data shows an increased contribution of the peak associated with oxidized Rh when the annealing temperature is increased. This suggests an incorporation of Rh atoms into the hematite lattice. After annealing the samples to 400 °C the metallic contribution visible in XPS could stem from leftover clusters on the surface.

Annealing at 500 °C results in a seemingly clean surface in STM and the disappearance of the remaining metallic contribution of the Rh 3d peak in XPS. The oxide peak maximum is situated at ≈ 309.6 eV for the undoped sample and at ≈ 309.3 eV for the ultra-low Ti-doped one, shifted by ≈ 1.5 eV, ≈ 1.1 eV and ≈ 1.3 eV respectively when compared to the peak position after deposition. This closely resembles the 1.2 eV shift between the Rh 3d metal and Rh(III) oxide peak given in literature [69].

The fact that the surface looks clean in STM while the XPS still shows a significant Rh contribution again heavily suggests an incorporation of Rh into the hematite lattice.

Preliminary DFT calculations were performed to discern the energetically most favourable position for incorporation, provided that the Rh atom substitutes for an iron lattice atom. The results show that the surface layer (layer 1) is significantly disfavoured with a substitution energy of 2.45 eV, while the first subsurface cation layer (layer 2) shows the lowest energy value with 1.93 eV. Going down further, the substitution energy rises again at the second subsurface layer (layer 3: 2.07 eV). The third subsurface layer shows a slightly lower substitution energy than the second one (layer 4: 2.05 eV). Going further into the bulk this value slowly increases towards the bulk value of 2.04 eV, but never reaching as low an energy level as in the first subsurface layer. The substitution energy is defined as the energy of the slab with one iron atom replaced by one Rh atom, minus the energy of the slab without that replacement. All energy values presented here are positive due to the higher oxygen affinity of iron compared to Rh.

The Vienna ab initio simulation package (VASP) was used for all DFT calculations, with the projector augmented wave method describing the electron-ion interactions. The Perdew, Burke, and Ernzerhof exchange-correlation functional was employed together with a Hubbard U ($U_{\text{eff}} = 4.0$) to treat the highly correlated Fe 3d electrons. The same U was applied for Rh atoms. Rh substitution was tested in (2×2) supercells on asymmetric slabs consisting of 20 atomic layers, using a Γ -centred k-mesh of $4 \times 4 \times 1$. The plane-wave basis-set cut-off energy was set to 450 eV, and all slabs were relaxed until the residual forces acting on ions were smaller than 0.02 eV/Å.

The DFT calculations suggest an incorporation of Rh into the first subsurface layer as the most energetically favourable position, while experimental data shows that an incorporation process is likely happening.

On magnetite, Rh has been shown to diffuse into the bulk at higher annealing temperatures (575 °C), vanishing completely in XPS spectra [71]. On hematite, annealing at 570 °C in UHV

(for the undoped sample, 550 °C for the ultra-low Ti-doped one) does not change the Rh XPS peak, suggesting that no significant bulk diffusion is happening at these temperatures.

It is yet unclear what happens to the displaced iron atoms during such an incorporation process. While it is conceivable that the observed clusters after annealing the surface to 400 °C are displaced iron atoms on the surface, this seems unlikely as iron has a higher oxophilicity than rhodium [72].

This suggests an incorporation into iron vacancies that either exist naturally or form during the annealing process due to bulk diffusion of iron atoms.

Experimentally, the existence of iron clusters could be detected using XPS, especially if there is a strong metallic contribution from the species. Sadly, the mounting geometry of the undoped sample makes data acquisition of the Fe 3d region without contributions of the steel (NiCrFe) sample plate impossible. On the ultra-low Ti-doped sample there also was a slight contribution from the NiCrFe sample plate and experiments with a high coverage have yet to be conducted. Extremely surface sensitive techniques such as low-energy ion scattering spectroscopy (LEIS) could also prove valuable in gathering more information about the clusters on the surface. Also, using a standard Ta or Mo sample plate instead of a NiCrFe one could help eliminate unwanted contributions in XPS.

Annealing the sample under reducing conditions at high temperatures (UHV, 570 °C for the undoped, 550 °C for the doped sample) usually leads to a change of the surface geometry to the (2×1) reconstruction. Interestingly, this process is hindered after Rh deposition. On the undoped crystal with 0.2 ML Rh, multiple annealing cycles were unsuccessful to prepare the (2×1) reconstruction, as confirmed with LEED measurements.

On the ultra-low Ti-doped thin film sample the experiment was repeated with 0.05 ML Rh coverage. As mentioned in Figure 35, the crystal surface does not have a homogenous temperature distribution. After the annealing process, the colder top half of the sample still showed a (1×1) pattern in LEED, while the hotter bottom half of the sample showed a (2×1) reconstruction. Without the presence of Rh, these preparation conditions always led to a (2×1) reconstruction on the whole sample surface, suggesting an influence of Rh regarding the phase transition also on the doped sample. STM images of the sample surface were recorded, confirming that the lower half of the crystal is dominated by the (2×1) reconstruction showing only few small patches of the (1×1) reconstruction, while the upper half showed mainly a (1×1) surface with some small regions of (2×1).

Assuming Rh incorporates into the lattice and substitutes iron atoms there, the oxidation state of such Rh atoms would be +3, akin to the Fe atoms which they replace. During the phase

transition to the (2×1) reconstruction, some Fe atoms change their oxidation state to +2. While this reduced state is not unusual for iron, occurring in both wüstite and magnetite, it is not as commonly found for Rh atoms. There are reports on chemical compounds with Rh in the +2 state, though this usually only occurs in organic molecules [73,74]. If it is energetically unfavourable for the Rh atoms to assume this reduced oxidation state, the presence of Rh in the hematite lattice could stabilize the (1×1) reconstruction at higher temperatures, preventing the usual change to the (2×1) reconstruction. Apparently, even higher sample temperatures still allow for the (2×1) to form. It is yet unknown how much energy is required to undergo this phase transition and how Rh affects this process. Also, calculations regarding the phase transition of the surface from (1×1) to (2×1) are complicated by the not yet fully understood (2×1) reconstruction. In the future, DFT will hopefully complement the experimental data and provide a more complete insight into this process.

It is possible that STM measurements can detect the subsurface dopants. Figure 34 and Figure 33 show STM data of the ultra-low Ti-doped sample surface after deposition 0.05 ML Rh and annealing at 400 °C in UHV conditions. The big cluster-like protrusion (marked in blue) shows a height of ≈ 200 pm, similar to the protrusions on the undoped sample with a Rh coverage of 0.2 ML (Figure 29). This could be a Rh cluster responsible for the metallic contribution in XPS. The smaller protrusions (marked in yellow) could have a different origin. The incorporated Rh atoms could locally modify the electronic properties of the surface, stabilizing the adsorption of other molecules such as water. This process has been shown to happen on a magnetite surface with subsurface nickel atoms [75]. Discernible as a third kind of surface feature, some sections of the zig-zag row appear slightly brighter (marked with red arrows). These features look similar to subsurface interstitials on magnetite and are associated with some subsurface defects that changes the electronic structure of the surface atoms. Possible candidates for such defects include subsurface oxygen vacancies or incorporated Rh atoms.

5.5 Summary and Outlook

The $\text{Fe}_2\text{O}_3(012)$ (1×1) surface was extensively studied using various surface science techniques. An overview on how to successfully perform STM and LEED on a poorly conductive surface was given. To achieve the necessary surface conductivity, hematite single crystals can either undergo several sputter and anneal cycles to reduce the subsurface layers, or doped thin films can be grown. The clean surfaces of samples with various Ti-doping levels were presented. The growth process – and the necessary target preparation process – of an ultra-low Ti-doped (0.03 at%) thin film was discussed. This system proved to be viable for surface science experiments and may provide a new standard for future experiments on hematite by combining the advantages of undoped samples (little dopant-induced surface defects, no “contamination” in spectroscopy techniques) with the advantages of doped thin film samples (flatness, ease to prepare and reproduce).

The intrinsic problem of scanning the surface with a negative sample bias was outlined. Multiple scans under such conditions lead to protrusions forming on the surface, suggesting that generally a positive sample bias should be used to study this surface in STM.

Preliminary results of surface defect generation by hydrogen deposition with subsequent annealing and by electron gun bombardment were presented. The techniques look promising regarding the generation surface oxygen vacancies and should be studied further in the future. A study of low Rh coverages (0.2 and 0.05 ML) on the hematite (012) (1x1) surface was presented. STM and XPS in combination with theory calculations were successfully applied to analyse the behaviour of the deposited Rh atoms at different sample temperatures.

It is theorized, that for small Rh coverages of 0.05 ML, the deposited atoms do not cluster at high sample annealing temperatures. Rh rather incorporates into the hematite lattice, possibly into the first subsurface layer. While higher coverages (0.2 ML) of Rh also eventually incorporate after annealing at high temperatures (500 °C), the increased height of the protrusions at lower temperature stages (300 °C, 400 °C) suggest a sintering process.

While the lack of large cluster formation at higher temperatures is beneficial when trying to generate single atom catalysis systems, a complete incorporation into the subsurface lattice may be problematic. Further studies about the changes of the local electronic properties after such an incorporation process are necessary.

Building on the work presented in this thesis, experiments combining metal deposition with a surface defect generation, or a co-adsorption of molecules such as water, are the next step towards stabilizing single catalytically active elements on this surface.

References

- [1] J.G. De Vries, S.D. Jackson, *Homogeneous and heterogeneous catalysis in industry*, Catal. Sci. Technol. 2 (2012) 2009. <https://doi.org/10.1039/c2cy90039d>.
- [2] Y. Lei, F. Mehmood, S. Lee, J. Greeley, B. Lee, S. Seifert, R.E. Winansl, W. Elám, R.J. Meyer, P.C. Redfern, D. Teschner, R. Schlögl, M.J. Pellin, L.A. Curtiss, S. Vajda, *Increased silver activity for direct propylene epoxidation via subnanometer size effects*, Science (80-.). 328 (2010) 224–228. <https://doi.org/10.1126/science.1185200>.
- [3] S. Vajda, M.J. Pellin, J.P. Greeley, C.L. Marshall, L.A. Curtiss, G.A. Ballentine, J.W. Elam, S. Catillon-Mucherie, P.C. Redfern, F. Mehmood, P. Zapol, *Subnanometre platinum clusters as highly active and selective catalysts for the oxidative dehydrogenation of propane*, Nat. Mater. 8 (2009) 213–216. <https://doi.org/10.1038/nmat2384>.
- [4] M. Turner, V.B. Golovko, O.P.H. Vaughan, P. Abdulkin, A. Berenguer-Murcia, M.S. Tikhov, B.F.G. Johnson, R.M. Lambert, *Selective oxidation with dioxygen by gold nanoparticle catalysts derived from 55-atom clusters*, Nature. 454 (2008) 981–983. <https://doi.org/10.1038/nature07194>.
- [5] X.F. Yang, A. Wang, B. Qiao, J. Li, J. Liu, T. Zhang, *Single-atom catalysts: A new frontier in heterogeneous catalysis*, Acc. Chem. Res. 46 (2013) 1740–1748. <https://doi.org/10.1021/ar300361m>.
- [6] A.A. Bolzan, C. Fong, B.J. Kennedy, C.J. Howard, *Structural Studies of Rutile-Type Metal Dioxides*, Acta Crystallogr. Sect. B Struct. Sci. 53 (1997) 373–380. <https://doi.org/10.1107/S0108768197001468>.
- [7] B.R. Chalamala, R.H. Reuss, K.A. Dean, E. Sosa, D.E. Golden, *Field emission characteristics of iridium oxide tips*, J. Appl. Phys. 91 (2002) 6141–6146. <https://doi.org/10.1063/1.1467959>.
- [8] M. Wang, S. Yao, M. Madou, *A long-term stable iridium oxide pH electrode*, Sensors Actuators, B Chem. 81 (2002) 313–315. [https://doi.org/10.1016/S0925-4005\(01\)00972-8](https://doi.org/10.1016/S0925-4005(01)00972-8).
- [9] M. Yagi, E. Tomita, T. Kuwabara, *Remarkably high activity of electrodeposited IrO₂ film for electrocatalytic water oxidation*, J. Electroanal. Chem. 579 (2005) 83–88. <https://doi.org/10.1016/j.jelechem.2005.01.030>.
- [10] C.C.L. McCrory, S. Jung, J.C. Peters, T.F. Jaramillo, *Benchmarking heterogeneous electrocatalysts for the oxygen evolution reaction*, J. Am. Chem. Soc. 135 (2013) 16977–16987. <https://doi.org/10.1021/ja407115p>.
- [11] N. Bestaoui, E. Prouzet, P. Deniard, R. Brec, *Structural and analytical characterization of an iridium oxide thin layer*, Thin Solid Films. 235 (1993) 35–42. [https://doi.org/10.1016/0040-6090\(93\)90239-L](https://doi.org/10.1016/0040-6090(93)90239-L).
- [12] H.J. Cho, H. Horii, C.S. Hwang, J.W. Kim, C.S. Kang, B.T. Lee, S.I. Lee, Y.B. Koh, M.Y. Lee, *Preparation and characterization of iridium oxide thin films grown by DC reactive sputtering*, Japanese J. Appl. Physics, Part 1 Regul. Pap. Short Notes Rev. Pap. 36 (1997) 1722–1727. <https://doi.org/10.1143/jjap.36.1722>.

- [13] M.A. El Khakani, M. Chaker, E. Gat, *Pulsed laser deposition of highly conductive iridium oxide thin films*, Appl. Phys. Lett. 69 (1996) 2027–2029. <https://doi.org/10.1063/1.116868>.
- [14] M.A. El Khakani, M. Chaker, *Reactive pulsed laser deposition of iridium oxide thin films*, Thin Solid Films. 335 (1998) 6–12. [https://doi.org/10.1016/S0040-6090\(98\)00862-1](https://doi.org/10.1016/S0040-6090(98)00862-1).
- [15] B.R. Chalamala, Y. Wei, R.H. Reuss, S. Aggarwal, B.E. Gnade, R. Ramesh, J.M. Bernhard, E.D. Sosa, D.E. Golden, *Effect of growth conditions on surface morphology and photoelectric work function characteristics of iridium oxide thin films*, Appl. Phys. Lett. 74 (1999) 1394–1396. <https://doi.org/10.1063/1.123561>.
- [16] S.W. Kim, S.H. Kwon, D.K. Kwak, S.W. Kang, *Phase control of iridium and iridium oxide thin films in atomic layer deposition*, J. Appl. Phys. 103 (2008) 1–7. <https://doi.org/10.1063/1.2836965>.
- [17] R.S. Chen, Y.S. Chen, Y.S. Huang, Y.L. Chen, Y. Chi, C.S. Liu, K.K. Tiong, A.J. Carry, *Growth of IrO₂ films and nanorods by means of CVD: An example of compositional and morphological control of nanostructures*, Chem. Vap. Depos. 9 (2003) 301–305. <https://doi.org/10.1002/cvde.200304153>.
- [18] R.S. Chen, Y.S. Huang, Y.M. Liang, D.S. Tsai, Y. Chi, J.J. Kai, *Growth control and characterization of vertically aligned IrO₂ nanorods*, J. Mater. Chem. 13 (2003) 2525–2529. <https://doi.org/10.1039/b305602n>.
- [19] R.S. Chen, Y.S. Huang, D.S. Tsai, S. Chattopadhyay, C.T. Wu, Z.H. Lan, K.H. Chen, *Growth of well aligned IrO₂ nanotubes on LiTaO₃(012) substrate*, Chem. Mater. 16 (2004) 2457–2462. <https://doi.org/10.1021/cm030668n>.
- [20] R.S. Chen, A. Korotcov, Y.S. Huang, D.S. Tsai, *One-dimensional conductive IrO₂ nanocrystals*, Nanotechnology. 17 (2006). <https://doi.org/10.1088/0957-4484/17/9/R01>.
- [21] M.J.S. Abb, B. Herd, H. Over, *Template-Assisted Growth of Ultrathin Single-Crystalline IrO₂(110) Films on RuO₂(110)/Ru(0001) and Its Thermal Stability*, J. Phys. Chem. C. 122 (2018) 14725–14732. <https://doi.org/10.1021/acs.jpcc.8b04375>.
- [22] T. Weber, J. Pfrommer, M.J.S. Abb, B. Herd, O. Khalid, M. Rohnke, P.H. Lakner, J. Evertsson, S. Volkov, F. Bertram, R. Znaiguia, F. Carla, V. Vonk, E. Lundgren, A. Stierle, H. Over, *Potential-Induced Pitting Corrosion of an IrO₂(110)-RuO₂(110)/Ru(0001) Model Electrode under Oxygen Evolution Reaction Conditions*, ACS Catal. 9 (2019) 6530–6539. <https://doi.org/10.1021/acscatal.9b01402>.
- [23] R. Rai, T. Li, Z. Liang, M. Kim, A. Asthagiri, J.F. Weaver, *Growth and termination of a rutile IrO₂(100) layer on Ir(111)*, Surf. Sci. 652 (2016) 213–221. <https://doi.org/10.1016/j.susc.2016.01.018>.
- [24] Y. Bian, T. Li, J.F. Weaver, *Structure and reactivity of iridium oxide layers grown on Ir(100) by oxidation at sub-ambient O₂ pressures*, J. Phys. D. Appl. Phys. 52 (2019). <https://doi.org/10.1088/1361-6463/ab32cc>.
- [25] Z. Liang, T. Li, M. Kim, A. Asthagiri, J.F. Weaver, *Low-Temperature activation of methane on the IrO₂ (110) surface*, Science (80-.). 356 (2017) 299–303. <https://doi.org/10.1126/science.aam9147>.

- [26] W.W. Pai, T.Y. Wu, C.H. Lin, B.X. Wang, Y.S. Huang, H.L. Chou, *A cross-sectional scanning tunneling microscopy study of IrO₂ rutile single crystals*, Surf. Sci. 601 (2007) 39–42. <https://doi.org/10.1016/j.susc.2007.04.227>.
- [27] G. Novell-Leruth, G. Carchini, N. López, *On the properties of binary rutile MO₂ compounds, M = Ir, Ru, Sn, and Ti: A DFT study*, J. Chem. Phys. 138 (2013). <https://doi.org/10.1063/1.4803854>.
- [28] D. González, J. Heras-Domingo, S. Pantaleone, A. Rimola, L. Rodríguez-Santiago, X. Solans-Monfort, M. Sodupe, *Water Adsorption on MO₂ (M = Ti, Ru, and Ir) Surfaces. Importance of Octahedral Distortion and Cooperative Effects*, ACS Omega. 4 (2019) 2989–2999. <https://doi.org/10.1021/acsomega.8b03350>.
- [29] D. Opalka, C. Scheurer, K. Reuter, *Ab Initio Thermodynamics Insight into the Structural Evolution of Working IrO₂ Catalysts in Proton-Exchange Membrane Electrolyzers*, ACS Catal. 9 (2019) 4944–4950. <https://doi.org/10.1021/acscatal.9b00796>.
- [30] M. Asadian, *Thermodynamic Analysis of ZnO Crystal Growth from the Melt*, J. Cryst. Process Technol. 03 (2013) 75–80. <https://doi.org/10.4236/jcpt.2013.33012>.
- [31] V. Pfeifer, T.E. Jones, J.J. Velasco Vélez, C. Massué, M.T. Greiner, R. Arrigo, D. Teschner, F. Girgsdies, M. Scherzer, J. Allan, M. Hashagen, G. Weinberg, S. Piccinin, M. Hävecker, A. Knop-Gericke, R. Schlögl, *The electronic structure of iridium oxide electrodes active in water splitting*, Phys. Chem. Chem. Phys. 18 (2016) 2292–2296. <https://doi.org/10.1039/c5cp06997a>.
- [32] S.J. Freakley, J. Ruiz-Esquius, D.J. Morgan, *The X-ray photoelectron spectra of Ir, IrO₂ and IrCl₃ revisited*, Surf. Interface Anal. 49 (2017) 794–799. <https://doi.org/10.1002/sia.6225>.
- [33] G.K. Wertheim, H.J. Guggenheim, *Conduction-electron screening in metallic oxides: IrO₂*, Phys. Rev. B. 22 (1980) 4680–4683. <https://doi.org/10.1103/PhysRevB.22.4680>.
- [34] J.I.J. Choi, W. Mayr-Schmölzer, F. Mittendorfer, J. Redinger, U. Diebold, M. Schmid, *The growth of ultra-thin zirconia films on Pd₃Zr(0 0 1)*, J. Phys. Condens. Matter. 26 (2014). <https://doi.org/10.1088/0953-8984/26/22/225003>.
- [35] Y. Bian, T. Li, J.F. Weaver, *Structure and reactivity of iridium oxide layers grown on Ir(100) by oxidation at sub-ambient O₂ pressures*, J. Phys. D. Appl. Phys. 52 (2019). <https://doi.org/10.1088/1361-6463/ab32cc>.
- [36] C.M. Chan, W.H. Weinberg, *Low-energy electron diffraction structural analysis of the (2 × 2) oxygen overlayer on the iridium (111) surface*, J. Chem. Phys. 71 (1979) 2788–2792. <https://doi.org/10.1063/1.438683>.
- [37] H. Zhang, A. Soon, B. Delley, C. Stampfl, *Stability, structure, and electronic properties of chemisorbed oxygen and thin surface oxides on Ir(111)*, Phys. Rev. B - Condens. Matter Mater. Phys. 78 (2008) 1–12. <https://doi.org/10.1103/PhysRevB.78.045436>.
- [38] A.J. Martínez-Galera, U.A. Schröder, F. Huttmann, W. Jolie, F. Craes, C. Busse, V. Caciuc, N. Atodiresei, S. Blügel, T. Michely, *Oxygen orders differently under graphene: New superstructures on Ir(111)*, Nanoscale. 8 (2016) 1932–1943. <https://doi.org/10.1039/c5nr04976h>.

- [39] O. Dulub, C. Di Valentin, A. Selloni, U. Diebold, *Structure, defects, and impurities at the rutile TiO₂(011)-(2 × 1) surface: A scanning tunneling microscopy study*, Surf. Sci. 600 (2006) 4407–4417. <https://doi.org/10.1016/j.susc.2006.06.042>.
- [40] S. Halpegamage, P. Ding, X.Q. Gong, M. Batzill, *Ordered Fe(II)Ti(IV)O₃ Mixed Monolayer Oxide on Rutile TiO₂(011)*, ACS Nano. 9 (2015) 8627–8636. <https://doi.org/10.1021/acs.nano.5b04125>.
- [41] S. Halpegamage, Z.H. Wen, X.Q. Gong, M. Batzill, *Monolayer Intermixed Oxide Surfaces: Fe, Ni, Cr, and V Oxides on Rutile TiO₂(011)*, J. Phys. Chem. C. 120 (2016) 14782–14794. <https://doi.org/10.1021/acs.jpcc.6b05186>.
- [42] S. Halpegamage, L. Bignardi, P. Lacovig, A. Kramer, Z.H. Wen, X.Q. Gong, S. Lizzit, M. Batzill, *An ordered mixed oxide monolayer formed by iron segregation on Rutile-TiO₂(011): Structural determination by x-ray photoelectron diffraction*, J. Phys. Chem. C. 120 (2016) 26414–26424. <https://doi.org/10.1021/acs.jpcc.6b09651>.
- [43] S. Halpegamage, M. Batzill, *Mixed oxides on rutile TiO₂ (011): Cr₂O₃ and Cu₂O*, J. Vac. Sci. Technol. A Vacuum, Surfaces, Film. 35 (2017) 061406. <https://doi.org/10.1116/1.5000333>.
- [44] J. Balajka, Interaction of Titanium Dioxide Surfaces with Liquid Water, TU Wien, 2018. <http://repositum.tuwien.ac.at/urn:nbn:at:at-ubtuw:1-115430>.
- [45] G.S. Parkinson, *Iron oxide surfaces*, Surf. Sci. Rep. 71 (2016) 272–365. <https://doi.org/10.1016/j.surfrep.2016.02.001>.
- [46] L.A. Marusak, R. Messier, W.B. White, *Optical absorption spectrum of hematite, α-Fe₂O₃ near IR to UV*, J. Phys. Chem. Solids. 41 (1980) 981–984. [https://doi.org/10.1016/0022-3697\(80\)90105-5](https://doi.org/10.1016/0022-3697(80)90105-5).
- [47] B. Iandolo, B. Wickman, I. Zorić, A. Hellman, *The rise of hematite: origin and strategies to reduce the high onset potential for the oxygen evolution reaction*, J. Mater. Chem. A. 3 (2015) 16896–16912. <https://doi.org/10.1039/c5ta03362d>.
- [48] K. Sivula, F. Le Formal, M. Grätzel, *Solar water splitting: Progress using hematite (α-Fe₂O₃) photoelectrodes*, ChemSusChem. 4 (2011) 432–449. <https://doi.org/10.1002/cssc.201000416>.
- [49] M. Rioult, R. Belkhou, H. Magnan, D. Stanescu, S. Stanescu, F. Maccherozzi, C. Rountree, A. Barbier, *Local electronic structure and photoelectrochemical activity of partial chemically etched Ti-doped hematite*, Surf. Sci. 641 (2015) 310–313. <https://doi.org/10.1016/j.susc.2015.01.002>.
- [50] W. Li, S.W. Sheehan, D. He, Y. He, X. Yao, R.L. Grimm, G.W. Brudvig, D. Wang, *Hematite-Based Solar Water Splitting in Acidic Solutions: Functionalization by Mono- and Multilayers of Iridium Oxygen-Evolution Catalysts*, Angew. Chemie - Int. Ed. 54 (2015) 11428–11432. <https://doi.org/10.1002/anie.201504427>.
- [51] B. Qiao, A. Wang, X. Yang, L.F. Allard, Z. Jiang, Y. Cui, J. Liu, J. Li, T. Zhang, *Single-atom catalysis of CO oxidation using Pt₁/FeO_x*, Nat. Chem. 3 (2011) 634–641. <https://doi.org/10.1038/nchem.1095>.

- [52] L. Li, A. Wang, B. Qiao, J. Lin, Y. Huang, X. Wang, T. Zhang, *Origin of the high activity of Au/FeO_x for low-temperature CO oxidation: Direct evidence for a redox mechanism*, *J. Catal.* 299 (2013) 90–100. <https://doi.org/10.1016/j.jcat.2012.11.019>.
- [53] B. Bing Chen, X. Bing Zhu, M. Crocker, Y. Wang, C. Shi, *FeO_x-supported gold catalysts for catalytic removal of formaldehyde at room temperature*, *Appl. Catal. B Environ.* 154–155 (2014) 73–81. <https://doi.org/10.1016/j.apcatb.2014.02.009>.
- [54] B. Qiao, J.X. Liang, A. Wang, C.Q. Xu, J. Li, T. Zhang, J.J. Liu, *Ultrastable single-atom gold catalysts with strong covalent metal-support interaction (CMSI)*, *Nano Res.* 8 (2015) 2913–2924. <https://doi.org/10.1007/s12274-015-0796-9>.
- [55] J. Lin, A. Wang, B. Qiao, X. Liu, X. Yang, X. Wang, J. Liang, J. Li, J. Liu, T. Zhang, *Remarkable performance of Ir₁/FeO_x single-atom catalyst in water gas shift reaction*, *J. Am. Chem. Soc.* 135 (2013) 15314–15317. <https://doi.org/10.1021/ja408574m>.
- [56] X. Sun, J. Lin, Y. Zhou, L. Li, Y. Su, X. Wang, T. Zhang, *FeO_x supported single-atom Pd bifunctional catalyst for water gas shift reaction*, *AIChE J.* 63 (2017) 4022–4031. <https://doi.org/10.1002/aic.15759>.
- [57] F. Li, Y. Li, X.C. Zeng, Z. Chen, *Exploration of high-performance single-atom catalysts on support M₁/FeO_x for CO oxidation via computational study*, *ACS Catal.* 5 (2015) 544–552. <https://doi.org/10.1021/cs501790v>.
- [58] J.X. Liang, X.F. Yang, A. Wang, T. Zhang, J. Li, *Theoretical investigations of non-noble metal single-atom catalysis: Ni₁/FeO_x for CO oxidation*, *Catal. Sci. Technol.* 6 (2016) 6886–6892. <https://doi.org/10.1039/c6cy00672h>.
- [59] R. Bliem, J. Pavelec, O. Gamba, E. McDermott, Z. Wang, S. Gerhold, M. Wagner, J. Osiecki, K. Schulte, M. Schmid, P. Blaha, U. Diebold, G.S. Parkinson, *Adsorption and incorporation of transition metals at the magnetite Fe₃O₄(001) surface*, *Phys. Rev. B - Condens. Matter Mater. Phys.* 92 (2015) 075440. <https://doi.org/10.1103/PhysRevB.92.075440>.
- [60] B. Arndt, R. Bliem, O. Gamba, J.E.S. Van Der Hoeven, H. Noei, U. Diebold, G.S. Parkinson, A. Stierle, *Atomic structure and stability of magnetite Fe₃O₄(001): An X-ray view*, *Surf. Sci.* 653 (2016) 76–81. <https://doi.org/10.1016/j.susc.2016.06.002>.
- [61] Y. Zhao, K.R. Yang, Z. Wang, X. Yan, S. Cao, Y. Ye, Q. Dong, X. Zhang, J.E. Thorne, L. Jin, K.L. Materna, A. Trimpalis, H. Bai, S.C. Fakra, X. Zhong, P. Wang, X. Pan, J. Guo, M. Flytzani-Stephanopoulos, G.W. Brudvig, V.S. Batista, D. Wang, *Stable iridium dinuclear heterogeneous catalysts supported on metal-oxide substrate for solar water oxidation*, *Proc. Natl. Acad. Sci. U. S. A.* 115 (2018) 2902–2907. <https://doi.org/10.1073/pnas.1722137115>.
- [62] J.E. Katz, X. Zhang, K. Attenkofer, K.W. Chapman, C. Frandsen, P. Zarzycki, K.M. Rosso, R.W. Falcone, G.A. Waychunas, B. Gilbert, *Electron small polarons and their mobility in iron (oxyhydr)oxide nanoparticles*, *Science* (80-.). 337 (2012) 1200–1203. <https://doi.org/10.1126/science.1223598>.
- [63] G. Franceschi, F. Kraushofer, M. Meier, G.S. Parkinson, M. Schmid, U. Diebold, M. Riva, *A model system for photocatalysis: Ti-doped Fe₂O₃ (1–102) single-crystalline films*, *Chem. Mater.* (2020). <https://doi.org/10.1021/acs.chemmater.9b04908>.

- [64] G. Franceschi, M. Wagner, J. Hofinger, T. Krajňák, M. Schmid, U. Diebold, M. Riva, *Growth of In_2O_3 (111) thin films with optimized surfaces*, Phys. Rev. Mater. 3 (2019) 1–10. <https://doi.org/10.1103/PhysRevMaterials.3.103403>.
- [65] M.A. Henderson, S.A. Joyce, J.R. Rustad, *Interaction of water with the (1 × 1) and (2 × 1) surfaces of $\alpha\text{-Fe}_2\text{O}_3(012)$* , Surf. Sci. 417 (1998) 66–81. [https://doi.org/10.1016/S0039-6028\(98\)00662-1](https://doi.org/10.1016/S0039-6028(98)00662-1).
- [66] F. Kraushofer, Z. Jakub, M. Bichler, J. Hulva, P. Drmota, M. Weinold, M. Schmid, M. Setvin, U. Diebold, P. Blaha, G.S. Parkinson, *Atomic-Scale Structure of the Hematite $\alpha\text{-Fe}_2\text{O}_3(11-02)$ “r-Cut” Surface*, J. Phys. Chem. C. 122 (2018) 1657–1669. <https://doi.org/10.1021/acs.jpcc.7b10515>.
- [67] M.A. Henderson, *Insights into the (1 × 1)-to-(2 × 1) phase transition of the $\alpha\text{-Fe}_2\text{O}_3(012)$ surface using EELS, LEED and water TPD*, Surf. Sci. 515 (2002) 253–262. [https://doi.org/10.1016/S0039-6028\(02\)01917-9](https://doi.org/10.1016/S0039-6028(02)01917-9).
- [68] L.Q. Wang, D.R. Baer, M.H. Engelhard, *Creation of variable concentrations of defects on $\text{TiO}_2(110)$ using low-density electron beams*, Surf. Sci. 320 (1994) 295–306. [https://doi.org/10.1016/0039-6028\(94\)90317-4](https://doi.org/10.1016/0039-6028(94)90317-4).
- [69] Y. Abe, K. Kato, M. Kawamura, K. Sasaki, *Rhodium and Rhodium Oxide Thin Films Characterized by XPS*, Surf. Sci. Spectra. 8 (2001) 117–125. <https://doi.org/10.1116/11.20010801>.
- [70] S. Peters, S. Peredkov, M. Neeb, W. Eberhardt, M. Al-Hada, *Size-dependent XPS spectra of small supported Au-clusters*, Surf. Sci. 608 (2013) 129–134. <https://doi.org/10.1016/j.susc.2012.09.024>.
- [71] Z. Jakub, J. Hulva, P.T.P. Ryan, D.A. Duncan, D.J. Payne, R. Bliem, M. Ulreich, P. Hofegger, F. Kraushofer, M. Meier, M. Schmid, U. Diebold, G.S. Parkinson, *Adsorbate-induced structural evolution changes the mechanism of CO oxidation on a Rh/ $\text{Fe}_3\text{O}_4(001)$ model catalyst*, (2020). <https://doi.org/10.1039/c9nr10087c>.
- [72] K.P. Kepp, *A quantitative scale of oxophilicity and thiophilicity*, Inorg. Chem. 55 (2016) 9461–9470. <https://doi.org/10.1021/acs.inorgchem.6b01702>.
- [73] R.L. Harlow, D.L. Thorn, R.T. Baker, N.L. Jones, *Structural determinations of chlorobis(triisopropylphosphine)rhodium compounds in the +2 and +3 oxidation states*, Inorg. Chem. 31 (1992) 993–997. <https://doi.org/10.1021/ic00032a014>.
- [74] M.E. Prater, L.E. Pence, R. Clérac, G.M. Finnis, C. Campana, P. Auban-Senzier, D. Jérôme, E. Canadell, K.R. Dunbar, *A remarkable family of rhodium acetonitrile compounds spanning three oxidation states and with nuclearities ranging from mononuclear and dinuclear to one-dimensional chains*, J. Am. Chem. Soc. 121 (1999) 8005–8016. <https://doi.org/10.1021/ja991130e>.
- [75] Z. Jakub, J. Hulva, F. Mirabella, F. Kraushofer, M. Meier, R. Bliem, U. Diebold, G.S. Parkinson, *Nickel doping enhances the reactivity of $\text{Fe}_3\text{O}_4(001)$ to water*, J. Phys. Chem. C. 123 (2019) 15038–15045. <https://doi.org/10.1021/acs.jpcc.9b02993>.